Available online at www.sciencedirect.com

ScienceDirect

Geochimica et Cosmochimica Acta 282 (2020) 55–75

Geochimica et Cosmochimica Acta

www.elsevier.com/locate/gca

Hydrogen generation and iron partitioning during experimental serpentinization of an olivine–pyroxene mixture

Thomas M. McCollom [a,*], Frieder Klein [b], Bruce Moskowitz [c,d], Thelma S. Berquó [e], Wolfgang Bach [f], Alexis S. Templeton [g]

[a] *Laboratory for Atmospheric and Space Physics, University of Colorado, Boulder, CO 80309, USA*
[b] *Woods Hole Oceanographic Institution, Wood Hole, MA 02543, USA*
[c] *Department of Earth and Environmental Sciences, University of Minnesota, Minneapolis, MN 55455, USA*
[d] *Institute for Rock Magnetism, University of Minnesota, Minneapolis, MN 55455, USA*
[e] *Department of Physics, Concordia College, Moorhead, MN 56562, USA*
[f] *Department of Geosciences, University of Bremen, 28334 Bremen, Germany*
[g] *Department of Geological Sciences, University of Colorado, Boulder, CO 80309, USA*

Received 30 August 2018; accepted in revised form 15 May 2020; available online 26 May 2020

Abstract

A series of laboratory experiments was conducted to investigate serpentinization of olivine–pyroxene mixtures at 230 °C, with the objective of evaluating the effect of mixed compositions on Fe partitioning among product minerals, H_2 generation, and reaction rates. An initial experiment reacted a mixture of 86 wt.% olivine and 14 wt.% orthopyroxene (Opx) with the same initial grain size for 387 days. The experiment resulted in extensive reaction (~53% conversion), and solids recovered at termination of the experiment were dominated by Fe-bearing chrysotile and relict olivine along with minor brucite and magnetite. Only limited amounts of H_2 were generated during the first ~100 days of the experiment, but the rate of H_2 generation then increased sharply coincident with an increase in pH from mildly alkaline to strongly alkaline conditions. Two shorter term experiments with the same reactants (26 and 113 days) produced a mixture of lizardite and talc that formed a thin coating on relict olivine and Opx grains, with virtually no generation of H_2. Comparison of the results with reaction path models indicates that the Opx reacted about two times faster than olivine, which contrasts with some previous studies that suggested olivine should react more rapidly than Opx at the experimental conditions. The models also indicate that the long-term experiment transitioned from producing serpentine ± talc early in the early stages to precipitation of serpentine plus magnetite, with brucite beginning to precipitate only late in the experiment as Opx was depleted. The results indicate that overall reaction of olivine and Opx was initially relatively slow, but reaction rates accelerated substantially when the pH transitioned to strongly alkaline conditions. Serpentine and brucite precipitated from the olivine-Opx mixture had higher Fe contents than observed in olivine-only experiments at mildly alkaline pH, but had comparable Fe contents to reaction of olivine at strongly alkaline pH implying that higher pH may favor greater partitioning of Fe into serpentine and brucite and less into magnetite. Despite the presence of brucite, dissolved silica activities during the long-term olivine-Opx experiment maintained levels well above serpentine-brucite equilibrium. Instead, silica activities converged on levels close to metastable equilibrium between brucite and olivine. It is proposed that silica levels during the experiment may have been regulated by exchange of SiO_2 between the fluid and a silica-depleted, brucite-like surface layer on dissolving olivine.

* Corresponding author.
E-mail address: mccollom@lasp.colorado.edu (T.M. McCollom).

https://doi.org/10.1016/j.gca.2020.05.016
0016-7037/

1. INTRODUCTION

Serpentinites are major components of the oceanic lithosphere and of ophiolites, and there is a long history of experimental studies conducted to understand the mineralogical and chemical changes that occur as ultramafic rocks undergo serpentinization (e.g., Martin and Fyfe, 1970; Moody, 1976a; Seyfried and Dibble, 1980; Wegner and Ernst, 1983; Janecky and Seyfried, 1986; Berndt et al., 1996; McCollom and Seewald, 2001; Seyfried et al., 2007; Malvoisin et al., 2012a,b; Klein et al., 2015; McCollom et al., 2016). In recent years, there has been an increased effort in both experimental and theoretical studies to understand the fate of Fe during serpentinization, which is closely related to the generation of molecular hydrogen (H_2) (e.g., Berndt et al., 1996; McCollom and Seewald, 2001; Seyfried et al., 2007; McCollom and Bach, 2009; Klein et al., 2009, 2013, 2014; Malvoisin et al., 2012a,b; Shibuya et al., 2015; McCollom et al., 2016; Grozeva et al., 2017). Interest in these topics has been stimulated in large part by the role of H_2 in promoting the activity of microbial communities and the abiotic synthesis of organic compounds in serpentinizing environments (see reviews by Schrenk et al., 2013, and McCollom and Seewald, 2007, 2013). In addition, the manner in which Fe is partitioned among the reaction products has a large effect on the amount of magnetite that is produced as serpentinization proceeds, which has a major impact on the evolution of magnetic properties of the oceanic crust over time (Toft et al., 1990; Oufi et al., 2002; Klein et al., 2014; Bonnemains et al., 2016).

The production of H_2 during serpentinization is intimately linked to the fate of Fe as the reaction proceeds, since it is the oxidation of ferrous Fe (Fe^{II}) derived from the primary minerals to ferric Fe (Fe^{III}) in the reaction products that generates H_2. In general terms, this process can be expressed as:

$$2[Fe^{II}O] + H_2O \rightarrow [Fe^{III}_2O_3] + H_2 \quad (1)$$

where $[Fe^{II}O]$ and $[Fe^{III}_2O_3]$ represent components of primary and secondary minerals, respectively. Evaluating the potential for H_2 production during serpentinization is complicated by the fact that there are many possible reservoirs for both Fe^{II} and Fe^{III} among the secondary products, including (but not limited to) members of the serpentine mineral group, magnetite, brucite, talc, and chlorite.

Despite the increased attention in recent years, several of the key factors that control the partitioning of Fe and generation of H_2 during serpentinization remain poorly understood. For example, laboratory experiments as well as studies of natural samples indicate that under some conditions serpentinization of ultramafic rocks can produce a steady increase in the amount of magnetite, while in other circumstances extensive reaction progress can occur with little or no magnetite production (Toft et al., 1990; Oufi et al., 2002; Bach et al., 2006; Seyfried et al., 2007; Malvoisin et al., 2012a,b; Klein et al., 2014; McCollom et al., 2016; Bonnemains et al., 2016). Similarly, rates of H_2 production measured in laboratory studies vary by orders of magnitude among different experiments, even when performed at similar temperatures (see McCollom et al., 2016 and references therein). While it appears likely that reaction temperature is a major contributor to these trends (e.g., McCollom and Bach, 2009; Klein et al., 2013; McCollom et al., 2016), there are additional factors that probably contribute as well. For instance, at various times many different environmental factors have been proposed to influence the manner in which Fe is partitioned among the products of serpentinization, including the Fe content of source minerals, the prevailing activity of silica, the evolving oxidation state, pH, the relative proportions and chemical composition of minerals in the protolith, and thermodynamic equilibrium among reaction products (e.g., Moody, 1976b; Evans and Trommsdorf, 1972; Frost and Beard, 2007; Evans, 2008; McCollom and Bach, 2009; Klein et al., 2013; McCollom et al., 2020; Mayhew and Ellison, 2020). However, these ideas remain largely untested by laboratory experiments.

Conceptually, it should be possible to use laboratory studies to evaluate how individual experimental parameters such as mineral compositions or silica activity affect the composition of product minerals during serpentinization. However, a substantial barrier in using results from existing studies for this purpose is that they have been performed using a broad variety of different experimental approaches with widely variable reaction conditions (temperature, pressure, reactant mineral and bulk composition, initial grain size, presence or absence of a vapor headspace, reactor materials, starting fluid composition and pH, etc.). These differences in reaction parameters make it difficult to directly correlate results between individual studies. Another problematic aspect is that, until very recently, few published studies have provided detailed data on the distribution of Fe among product minerals or measured the amount of H_2 generated during the experiments. As a consequence, it is difficult to compare the results of the various experimental studies with one another, or to use the results of these studies to form a coherent understanding of how reaction outcomes vary depending on specific reaction parameters.

The present investigation is part of a larger study that was undertaken to address this issue by performing multiple experiments under similar conditions while systematically varying a single reaction parameter. Comparison of the results among experiments then allows for an examination of how variation in individual parameters affected the outcome of the reaction. In the first report from this study, a series of experiments was conducted to examine the effect of temperature on serpentinization of olivine, with experiments conducted over the range of 200–320 °C (McCollom et al., 2016). In the present report, this experimental series is expanded to examine the impact of including orthopyroxene (Opx) along with olivine among the mineral reactants. After olivine, Opx it generally the next most abundant mineral in peridotites and is a major contributor to serpentinization reactions (e.g., Klein et al., 2013). To facilitate direct comparison with the olivine-only experiments, reaction conditions were kept as similar as possible to those used by McCollom et al. (2016) except for the addition of Opx. Owing to time constraints, the

experiments reported here were performed only at 230 °C, but the results allow for evaluation of how inclusion of Opx influences reaction pathways, partitioning of Fe, and generation of H_2. A companion paper investigates the impact of pH on reaction rates (McCollom et al., 2020) and an additional study that examines reaction of a natural harzburgite under similar conditions is forthcoming.

2. METHODS

A series of four experiments were conducted for this study, as summarized in Table 1. The study included experiments with olivine-Opx mixtures encompassing a range of reaction times (620–9287 h), as well as one experiment that included only Opx as reactant. In the experiments, powdered mineral substrates were heated in the presence of NaCl- and $NaHCO_3$-bearing aqueous solutions. Production of dissolved H_2 and other changes in fluid composition were monitored at intervals during the experiments. Solids were recovered at the end of the experiments and analyzed for their mineral and chemical composition. Methods used to prepare the reactants and to analyze the fluids and solid reaction products are summarized below, with additional details provided in the supplemental materials.

All experiments were conducted in a flexible-cell hydrothermal apparatus using a gold reaction cell with titanium fittings (Supplemental Fig. S1; Seyfried et al., 1987). The reaction cell is contained within a stainless steel pressure housing, with water used as an external pressurizing fluid. The flexibility of the gold reaction cell allows fluids to be sampled without loss of pressure and eliminates the presence of a vapor headspace so that reactions are confined to the aqueous phase. The cell is equipped with a capillary tube attached to a valve through which fluid samples were taken at intervals during the experiments in order to monitor reaction progress over time. All titanium fittings that were exposed to reactants were combusted in air for at least 48 h at 400 °C prior to use in the experiments in order to form a relatively inert TiO_2 surface layer. Experiments were conducted at a pressure of 35 MPa.

To approximate seawater salinity, the initial fluid for the experiments contained 485 mmol NaCl/kg. In order to investigate possible carbon reduction and hydrocarbon formation during the experiments, a source of dissolved inorganic carbon (19.4 mmol $NaHCO_3$/kg) was also included. Analysis of reduced carbon compounds in the experiments is discussed elsewhere (McCollom, 2016). The initial water:rock mass ratio ranged from 1.8 to 2.6, although the ratio within the reaction vessel decreased during individual experiments as fluid aliquots were removed for chemical analysis and as water was incorporated into secondary phases.

The experiments were conducted using olivine and Opx powders that were both sieved to achieve grain sizes between 53 and 212 μm and washed repeatedly with deionized water to remove small particulates. The minerals were pulverized by hand with a ceramic mortar and pestle, always avoiding the use of metal tools that might result in contamination of the reactants with particles of metal that could generate H_2 during heating. The minerals used in the experiments were purchased from Excalibur Minerals (Charlottesville, PA, USA). Chemical compositions of the reactant minerals are summarized in Table 2.

The experiments were conducted by combining separately prepared olivine and orthopyroxene (Opx) powders that were mixed thoroughly prior to the experiment. The olivine used in these experiments was from San Carlos, Arizona. Only olivine crystals larger than ~4 mm in diameter were used to prepare the reactant minerals, and were hand-picked under a binocular microscope to exclude grains with obvious signs of weathering or inclusions of other minerals. Inspection of the prepared olivine reactant by scanning electron microscopy (SEM) coupled with energy-dispersive X-ray spectroscopy (EDS) indicated the minerals were >99% pure, but included trace amounts of Opx, clinopyroxene (Cpx), and Cr-bearing spinel. The Opx used in the experiments was from Bamble, Norway (Closmann et al., 1996). The first experiment conducted for this study was OlivOpx230 (Table 1), and close inspection of the Opx reactant used for that experiment after it was begun revealed that it contained minor amounts of contaminants, including ~6 vol.% quartz, ~4 vol.% Ca-phosphate (probably chlorapatite), ~4 vol.% talc, and ~2 vol.% albite. For subsequent experiments using this material, the minerals were more scrupulously separated during preparation to remove contaminants, and inspection by SEM-EDS indicated the starting Opx contained less than 1 vol.% of contaminating phases. Magnetization analysis indicated the Opx reactant contained 0.15 wt.% magnetite while the olivine was weakly magnetic (~60 times less than Opx) with no evidence for magnetite.

At intervals throughout the experiments, several fluid aliquots (0.3–1 g each) were taken directly into gas-tight glass syringes and analyzed for dissolved volatile species including H_2, total dissolved CO_2 ($\Sigma CO_2 = CO_{2(aq)} + HCO_3^- + CO_3^{2-}$), CH_4, and C_2-C_6 hydrocarbons. These compounds were measured by gas chromatography (GC) with thermoconductivity detection (TCD) or flame ioniza-

Table 1
Summary of experimental parameters.

Experiment	Target Temp. (°C)	Duration (h)	Mineral reactants	Initial fluid (g)	Initial W:R[#]
Opx230	230	2348	9.0 g Opx	45.8	2.2
OlivOpx230	230	9287	21.0 g Olivine + 3.5 g Opx	44.0	1.8
OlivOpx230med	230	2709	18.0 g Olivine + 3.2 g Opx	45.4	2.1
OlivOpx230short	230	620	20.0 g Olivine + 3.5 g Opx	43.8	1.9

[#] Water:rock ratio at start of experiment.

Table 2
Chemical compositions of starting minerals and reaction products determined by electron microprobe analysis.

Oxide (wt.%)	SC Olivine	Bamble Opx	Oliv230[#] Chrysotile	OlivOpx230 Chrysotile (n = 7)	OlivOpx230 Brucite (n = 7)	Opx230 Lizardite/ talc (n = 8)	Opx230 Talc (n = 13)
SiO_2	40.6	56.9	26.2	36.0 (1.9)	0.17 (0.30)	41.6 (2.2)	59.7 (2.4)
TiO_2	<0.01	0.06	<0.01	0.03 (0.03)	0.01 (0.01)	0.03 (0.03)	0.03 (0.03)
Al_2O_3	0.03	0.14	0.09	0.25 (0.08)	0.19 (0.11)	0.16 (0.03)	0.18 (0.10)
Cr_2O_3	<0.01	0.01	<0.01	0.02 (0.01)	<0.01	0.01 (0.01)	0.01 (0.01)
FeO	8.9	9.5	1.05	6.2 (0.8)	15 (2.4)	6.1 (0.6)	1.20 (0.37)
MgO	50.1	32.8	29.0	34.0 (1.2)	54 (3.6)	23.2 (1.2)	29.6 (1.4)
MnO	0.14	0.08	0.03	0.08 (0.04)	0.55 (0.23)	0.04 (0.03)	0.01 (0.01)
CaO	0.07	0.28	0.01	0.03 (0.02)	0.01 (0)	0.05 (0.01)	0.02 (0.01)
Na_2O	–	0.03	0.02	0.09 (0.05)	<0.01	0.19 (0.07)	0.04 (0.02)
K_2O	–	<0.01	0.02	<0.01	<0.01	0.07 (0.06)	<0.01
NiO	0.38	0.02	–	0.17 (0.15)	0.34 (0.11)	0.02 (0.02)	0.02 (0.02)
Cl	–	<0.01	0.08	0.15 (0.03)	0.04 (0.01)	–	–
Total	100.1	100.4	56.6	77 (3.5)	70 (5.4)	71.5 (2.8)	90.9 (2.7)
Mg#	91	86	98 (0.1)	91 (0.9)	87 (1.7)	88 (0.8)	98 (0.7)
(Mg + Fe):Si*				1.52	n/a	0.94	0.75

Data for reaction products are average values (n = number of analyses) with standard deviation in parentheses. *Molar ratio. [#]Data for chrysotile from olivine-only experiment at 230 °C (McCollom et al., 2016).

tion detection (FID) following a headspace extraction. For the headspace extraction, 1 ml of carrier gas (N_2 for the H_2 analysis or He for CO_2/hydrocarbons) was injected into the sample syringe from another gas-tight syringe, and the sample syringe was then agitated for about one minute to ensure complete transfer of volatiles into the gas phase. The gas was then transferred back to the other syringe and injected into the GC. In most cases, the reported H_2 concentrations are averages of 3–4 separate fluid aliquots, while other dissolved gases were typically only measured for a single aliquot to conserve fluid. For comparative purposes, the measured H_2 concentrations were normalized to the total number of moles generated per gram of reactant minerals to account for variations in the amounts of solids used in different experiments and for the changing mass of fluid present in the reaction vessel as aliquots are removed during sampling (that is, as the fluid is depleted, the same amount of H_2 production results in a greater increase in concentration). Only trace amounts (<1 μmol kg^{-1}) of C_2-C_6 hydrocarbons were observed in any of the experiments, so individual results are not reported. Estimated errors for volatile analyses are ±5%. Fluid aliquots remaining after extraction of volatiles were used for measurements of pH, total dissolved SiO_2, and major elements. More detailed methods for fluid analyses are provided in the Supplemental Materials.

At termination of the experiments, the solids were removed, filtered, and rinsed with DI water. The solids were characterized with a variety of methods including scanning electron microscopy coupled with energy-dispersive X-ray spectroscopy (SEM-EDS), X-ray diffraction (XRD), electron microprobe analysis (EMPA), Raman spectroscopy, thermogravimetric analysis (TGA), and magnetic methods (see Supplemental Materials for analytical details). To obtain additional information on the distribution of Fe among secondary phases, Mössbauer spectroscopy (MB) was also performed on the reaction products. In order to focus on secondary products, XRD and MB analyses were performed on materials that had been separated from remaining reactant minerals by sonication of the reacted solids in ethanol followed by removal of the suspended finer particles. A strong magnet was used to exclude magnetite from the separated fraction.

Reaction path models, fluid speciation calculations, and mineral stability diagrams were utilized to aid in the interpretation of the experimental data. The reaction path models were performed with the software package EQ3/6, version 7.2b (Wolery and Jarek, 2003) using methods described in McCollom and Bach (2009). The thermodynamic database used for the calculations is described in McCollom and Bach (2009) and Klein et al. (2013). The database was constructed for a constant pressure of 35 MPa and includes solid solution models for a number of minerals including serpentine and brucite. Most solid solutions included in the models assume ideal molecular mixing, but the serpentine solid solution assumes ideal site mixing with a site parameter of 2.5 with three endmembers (chrysotile, greenalite, and cronstedtite) (Klein et al., 2013).

Fluid speciation calculations to estimate in situ pH and silica activity were performed in two steps using EQ3. First, the fluid was speciated at 25 °C using the measured fluid compositions, including the room temperature pH, and adjusted for charge balance with Na. The total dissolved Na calculated at 25 °C was then used with other measured concentrations to respeciate the fluid at the reaction temperature, with charge balance determining the in situ pH. In those cases where Mg, Ca, and Fe were below detection limits, the total dissolved abundance of these elements were assumed to be 1 μmol kg^{-1}, 1 μmol kg^{-1}, 0.1 μmol kg^{-1}, respectively.

Mineral stability diagrams were constructed using the computer program Geochemist's Workbench, version 11

(GWB). The same 35 MPa database used for the EQ3/6 calculations was converted to GWB format for these calculations. However, because GWB does not provide for inclusion of solid solutions, thermodynamic parameters for solid solutions of chrysotile and brucite were calculated manually and entered into the database as discrete mineral phases, assuming ideal mixing of the endmembers.

3. RESULTS

Results of individual experiments are discussed in the following subsections. Table 2 provides chemical compositions of the major mineral products, Table 3 summarizes the most salient experimental results, and detailed analysis of fluid compositions during the experiments are provided in Supplemental Table S1.

3.1. Orthopyroxene only experiment (Opx230)

To provide context for interpretation of experiments combining both olivine and Opx, an initial experiment was performed that reacted only Opx with an aqueous solution for 2348 h (98 d) at 230 °C (Opx230). The composition of the fluid measured at several intervals during heating is listed in Supplemental Table S1. Throughout this experiment, the concentration of $H_{2(aq)}$ remained at very low levels close to the detection limit (~4 μmol kg^{-1}), while total dissolved silica (ΣSiO_2) maintained relatively constant concentrations near 1.8 mmol kg^{-1}. The measured room-temperature pH ($pH_{25°C}$) was circumneutral during the experiment, but the calculated in situ pH ($pH_{in\ situ}$) was mildly alkaline at ~7.2 (neutral pH at the experimental conditions is ~5.5). The concentration of Ca increased steadily during the reaction from 40 to 160 μmol kg^{-1}, while dissolved Mg, Fe, Al, and K were below detection limit (<~1 μmol kg^{-1}). Concentrations of dissolved Na, Cl and ΣCO_2 remained constant at their initial levels.

Examination of the reaction products showed that Opx only partially reacted during the experiment. Remnants of the reactant Opx were covered with a rind of secondary products that readily peeled off during drying (Fig. 1a). The rind was composed of a network of sheet-like materials oriented perpendicular to the surface of the Opx and coalescing into honeycomb-like structures (Fig. 1a & b). Inspection of the secondary products by SEM and other methods indicated that they were homogenous throughout the sample.

Most measurements of the secondary products from this experiment by Raman spectroscopy yielded bands that corresponded to both lizardite and talc, indicating that the alteration rinds were composed of an intimate mixture of these two minerals (Supplemental Fig. S2). In some spots, however, Raman analyses produced only bands corresponding to talc (Supplemental Fig. S2). Analysis of the products by XRD also indicated the presence of both talc and serpentine, but the peaks corresponding to these minerals are broad and muted, suggesting that the materials are poorly crystalline (Supplemental Fig. S3). In some areas, dense accumulations of an Fe-rich phase were observed on the undersides of the alteration rinds where they had been in contact with unreacted Opx (Fig. 1c). Raman analysis indicated these deposits included hematite, but additional Fe phases may have also been present (Supplemental Fig. S4).

Results of thermogravimetric analysis for this experiment are shown in Fig. 2b and summarized in Table 4. The reacted solids from this experiment exhibited a continuous weight loss between 450 °C and 850 °C, with a total loss of 0.63 wt.%. This weight loss was attributed to dehydration of lizardite and talc, but the lack of a clear plateau in the weight loss profile made it uncertain how much was attributable to each mineral. Consequently, it was assumed that all weight loss below 720 °C was attributable to lizardite while loss above this temperature was attributed to talc. Based on these results, it was estimated that ~7.3 wt. % of the original Opx was converted to secondary products during the experiment.

Analysis of the alteration rind by EMPA produced two distinct compositional populations, with one population evidently corresponding to a mixture of lizardite and talc while the other represents pure talc (Table 2). The lizardite/talc mixture has an apparent Mg# = 88

Table 3
Summary of experimental results, with data from other studies shown for comparison.

Experiment	Target Temp. (°C)	Duration (h)	Final H_2 conc. (mmol/kg)	Total H_2 generated (μmol/g minerals)	Mg#		wt.% Mag	Estimated % reaction*
					Srp	Brc		
Opx230	230	2348	0.004	0.005	88 (0.8)	–	–	7.3
OlivOpx230	230	9287	61.	90.7	91 (0.9)	87 (1.7)	1.52	53.
OlivOpx230med	230	2709	0.008	<0.016	–	–	<0.01	1.9
OlivOpx230short	230	620	0.020	<0.03	–	–	–	–
Oliv230[#]	230	8183	5.8	7.9	98 (0.1)	92 (1.6)	0.37	4.9
Oliv230pH[†]	230	2972	47.	105.	93 (0.9)	78 (1.0)	1.6	70.

*Percent of total primary minerals reacted determined from TGA results (see Supplemental Materials for details). Numbers in parentheses are standard deviations. "–" = not determined or not present. Srp = serpentine, Brc = brucite, Mag = magnetite. [#]Data for olivine-only experiment at circumneutral pH ($pH_{25°C} \approx 9$) from McCollom et al. (2016). [†]Data for olivine-only experiment at strongly alkaline pH ($pH_{25°C} \approx 12$) from McCollom et al. (2020).

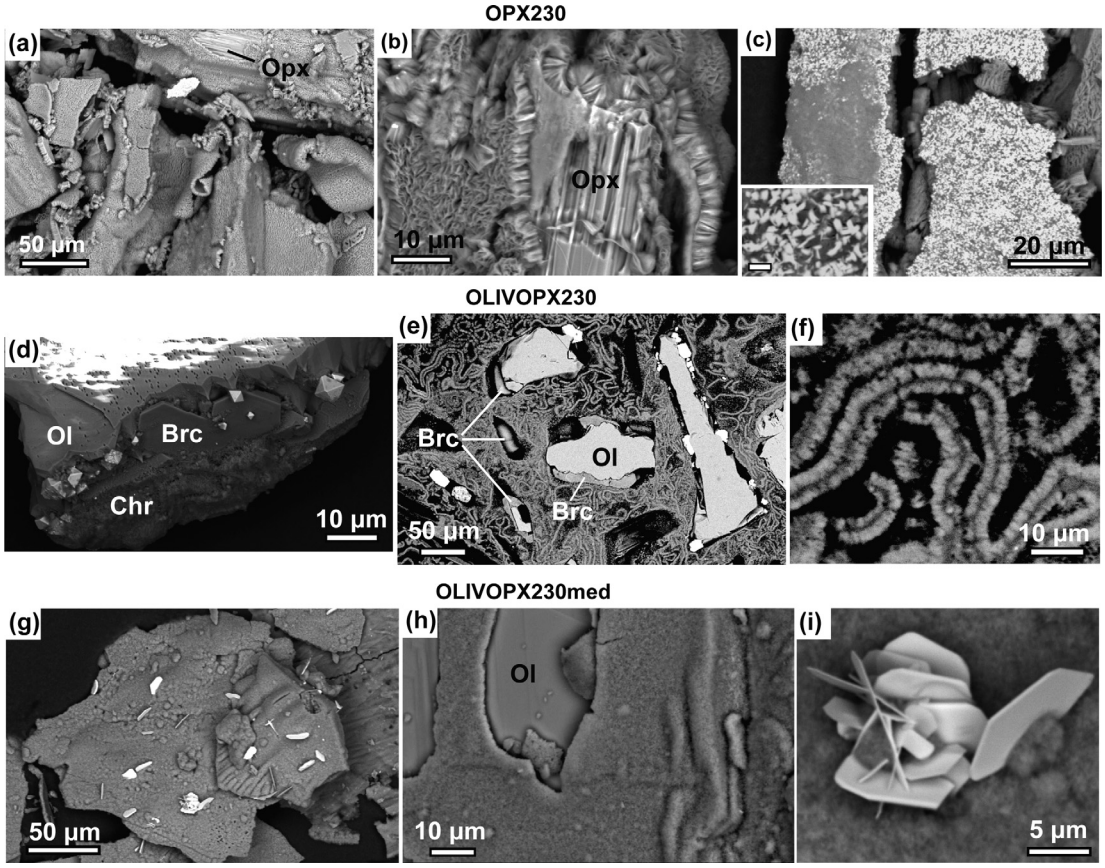

Fig. 1. Back-scattered electron (BSE) images of representative reaction products from 230 °C experiments. (a-c) Experiment Opx230. Panels (a) and (b) show rinds of alteration minerals on surface, with Opx exposed where the rind has peeled off. (c) Underside of reaction rind peeled off of Opx crystal showing Fe-oxide/oxyhydroxide deposits (bright areas in BSE), shown in expanded view in inset (scale bar is 1 μm). The bright area near top of (a) is another example of these Fe-oxide/oxhydroxide deposits. (d-f) Experiment OlivOpx230. (d) Reaction products including fibrous chrysotile (Chr), platy brucite (Brc), and octahedral magnetite on surface of reacting olivine (ol). Bright area at top of image is charging from the electron beam. (e) Cross-section of reaction products, showing partially reacted olivine, fibrous chrysotile, and brucite in close association with the olivine. Bright areas are magnetite. (f) Close-up of chrysotile from upper left corner of panel (e). (g-i) Experiment OlivOpx230med. (g) Overview of rind of secondary minerals accumulated on relict primary minerals. (h) Closer view of alteration rind, with relict olivine exposed where the rind has peeled off. (i) Close-up of platy, hexagonal Fe-oxide mineral from bottom of panel (g), presumably hematite.

[Mg# = 100 × Mg/(Mg + Fe), molar basis], similar to that of the Opx reactant, and a molar (Mg + Fe):Si ratio of 0.94, between the expected ratios for lizardite (1.5) and talc (0.75). The talc contains little Fe (Mg# = 98), suggesting that most of the Fe resides in the lizardite component. Three doublets were identified in the Mössbauer spectra for products from this experiment, with two peaks assigned to Fe^{II} and one peak to Fe^{III} (Table 5; Supplemental Fig. S5). The hyperfine parameters for the main Fe^{II} doublet is similar to that of the M2 site of the reactant Opx, but inspection of the sample prepared for MB analysis indicated very little Opx was present in the materials used for the analysis (Supplemental Fig. S6). Consequently, this doublet appears to be attributable to talc. The other Fe^{II} doublet, which appears as a shoulder on the main doublet, is attributable to Fe^{II} associated with the lizardite/talc mixture, while the Fe^{III} doublet is consistent with hyperfine parameters for the octahedral site of lizardite. In addition to the three doublets, a ferric singlet (~5% of the total spectra) was needed to improve the quality of the fit. The identity of the phase responsible for the singlet is uncertain, but it may be due to the Fe-oxide/hydroxide observed on the underside of the alteration rind in some areas (Fig. 1c). The MB results indicate that Fe^{III} components comprise about 25% of the total Fe in the alteration products (Table 5).

3.2. Long-term olivine plus orthopyroxene experiment (OlivOpx230)

The first experiment to combine Opx with olivine (OlivOpx230) was performed at 230 °C and was heated for 9287 h (387 d). Because of the long duration of the experiment, additional fluid (17.4 g) was injected into the experiment after 4512 h to replace fluid removed during sampling (the composition of the injected fluid was the same as that of the initial fluid). The evolution of fluid composition during the experiment is listed in Sup-

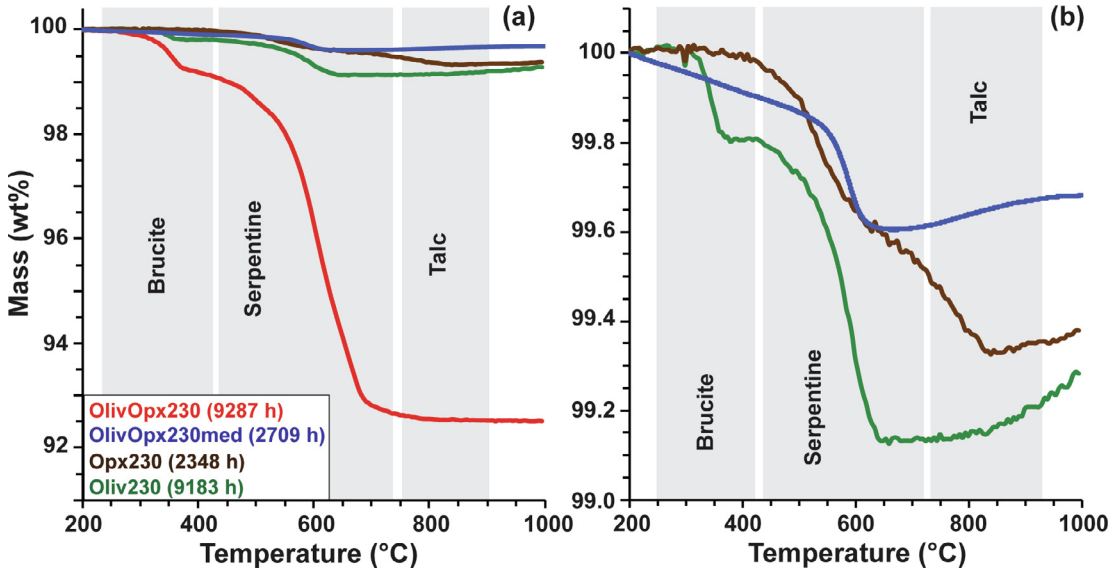

Fig. 2. Results of thermogravimetric analysis of reacted solids for laboratory experiments, with selected results displayed on an expanded scale in (b). Shown for comparison are results for an olivine-only experiment (Oliv230; McCollom et al., 2016). Mass loss between 250 °C and 430 °C is assigned to brucite, 450–730 °C assigned to serpentine (Viti, 2010), and 730–900 °C assigned to talc.

Table 4
Results of thermogravimetric analyses and magnetization measurements.

	Opx230 Opx only	Oliv230* Olivine only	OlivOpx230 Olivine + Opx	OlivOpx230med Olivine + Opx
TGA weight loss (%):				
Serpentine	0.41	0.66	6.6	0.27
Brucite	0	0.058	0.87	0
Talc	0.22	0	0	0
Secondary minerals (wt.%):				
Serpentine	3.3	5.0	52	2.1
Brucite	0	0.2	3.0	0
Talc	4.6	0	0	0
Magnetite[#]	0	0.37	1.52	0
Total reaction (%)[†]	7.3	4.9	53	1.9
Duration (h)	2348	8183	9287	2709

[*] Results from McCollom et al. (2016). This olivine-only experiment lasted 8183 h (vs. 2348 h for Opx230) yet resulted in far less total reaction.
[#] From magnetization measurements.
[†] Estimated percent of total primary minerals reacted, by mass. See Supplemental Materials for methods.

plemental Table S1, with the most salient fluid components illustrated in Fig. 3.

The production of H_2 during experiment OlivOpx230 is displayed in Fig. 3a, where it can be seen that H_2 production can be divided into three stages. The amount of H_2 produced increased only very gradually during the first 1344 h of heating, but then began to increase at a higher rate. Following the sample at 3359 h, the rate of H_2 production increased even further, and remained at this rate for the remainder of the experiment. Although additional fluid was injected at 4512 h, the steep increase occurred prior to this injection and continued at a steady rate afterwards, indicating that the injection had little or no impact on H_2 generation.

The room-temperature pH of the fluid was circumneutral during the first 3359 h of the experiment, but then increased steeply to strongly alkaline values above 10.5 (Fig. 3b). There was a slight decrease in $pH_{25°C}$ immediately following the injection of additional fluid, but it quickly recovered to a value above 11. The calculated $pH_{in\ situ}$ during the experiment was mildly alkaline during the first 3359 h, but then increased to more strongly alkaline conditions with values above 8.5 for the remainder of the experiment (Fig. 3b). Total dissolved SiO_2 exceeded 1900 μmol kg^{-1} in the first fluid sample, but thereafter decreased steadily until reaching 100 μmol kg^{-1} at 4488 h (Fig. 3c). During the remainder of the experiment, ΣSiO_2 concentrations remained relatively constant in the 46–

Table 5
Room-temperature hyperfine magnetic Mössbauer parameters for serpentine minerals in experimental samples and for reactant minerals.

Sample	QS (mm/s)	IS (mm/s)	%*	Assignment
Opx230	2.11	1.14	56	Fe^{II} (talc)
	2.69	1.11	19	Fe^{II} (serp)
	0.94	0.32	19	Fe^{III} (oct; serp)
	0	0.08	6	Fe^{III} (Fe-ox?)
Oliv230#	2.86	1.18	76	Fe^{II} (serp)
	0.66	0.28	24	Fe^{III} (oct; serp)
OlivOpx230	2.66	1.17	85	Fe^{II} (serp)
	0.89	0.15	15	Fe^{III} (oct; serp)
Bamble Opx	2.05	1.13	51	Fe^{II} (M2)
	1.81	1.00	49	Fe^{II} (M1)
SC olivine	3.00	1.18	100	Fe^{II}

* Relative abundances of Fe^{II} and Fe^{III} in the silicate component. Peak assignments for Fe^{III} in serpentine minerals correspond only to the octahedral (oct) site; no Fe^{III} was detected in the tetrahedral site for these samples.
# From McCollom et al. (2016).

100 μmol kg^{-1} range. Concentrations of dissolved Mg and Ca up to several hundred μmol kg^{-1} were observed during the first 3359 h of the experiment, but were below detection after this time (Supplemental Table S1). Potassium was present in the fluid at several hundred μmol kg^{-1} throughout the experiment, while Fe was always below detection. Presumably, the K observed in the fluid in this and other experiments is derived from a trace contaminant since neither the olivine nor Opx contained appreciable amounts of this element.

Inspection of the solids following termination of the experiment indicated that the alteration products were dominated by serpentine, magnetite, and brucite (Fig. 1d-f). Also observed were small amounts of carbonates, Ca-phosphate, and trace amounts of what appeared to be native metal phases (specifically, NiFe-alloy and native Pt; see Supplemental Fig. S8). Along with these products, a substantial fraction of the original olivine remained, but no remaining Opx was found. In addition, although small amounts of quartz and albite were present in the Opx reactant used for this experiment (<1.5 wt.% of total reactants), neither of these minerals was found during extensive inspection of the solids following reaction. Thermogravimetric analysis of the reacted solids resulted in a net weight loss of ~7.5 wt.%, which was predominantly attributable to decomposition of chrysotile and brucite (Fig. 2a). Based on the TGA results, ~53 wt.% of the starting minerals reacted during the experiment, indicating that ~45% of the original olivine and essentially all of the Opx had dissolved (Table 4).

Serpentine formed thick mats of elongated fibers that filled void spaces between remnant olivine crystals (Fig. 1e). In contrast to the Opx230 results, XRD analysis of the secondary products of this experiment indicates sharp peaks for the serpentine phase (Supplemental Fig. S3). The fibrous nature and Raman spectral signature (Supplemental Fig. S2) indicates that the serpentine is predominantly chrysotile. Analysis of chrysotile by EMPA indicated it contains a significant amount of Fe with an Mg# = 91 (Table 2), and thorough inspection of the reacted solids by both EMPA and EDS indicated the chrysotile has a uniform composition throughout the products. Mössbauer spectroscopy indicated the presence of both Fe^{II}

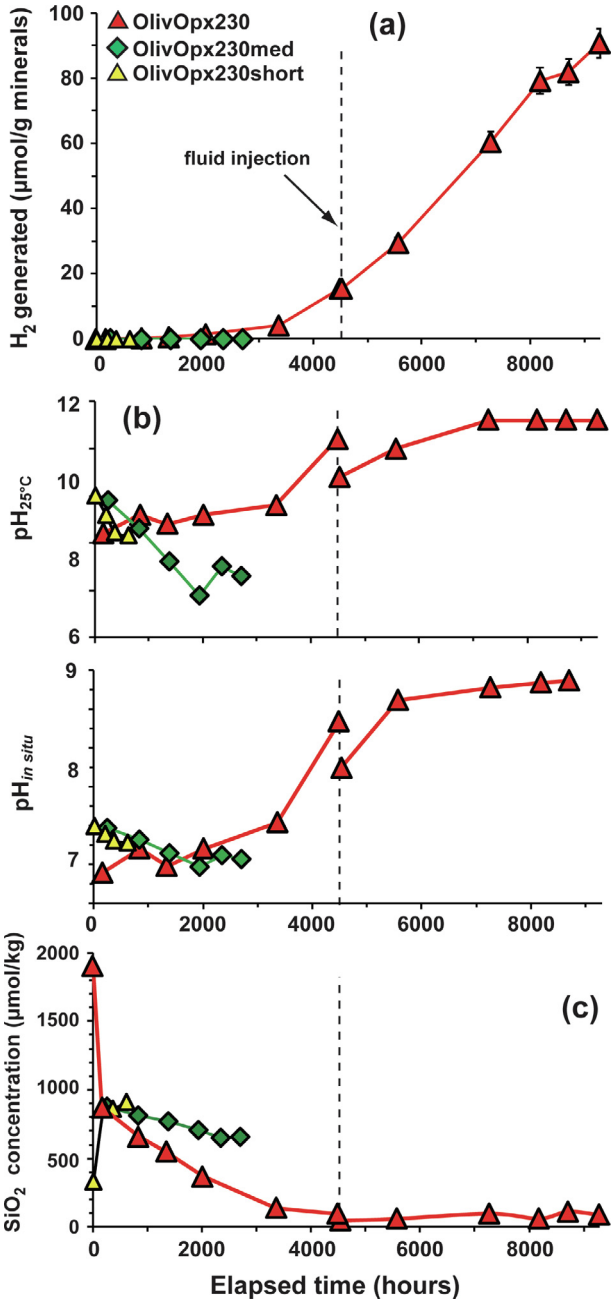

Fig. 3. Fluid compositions during olivine plus Opx mixture experiments at 230 °C. (a) Total amount of H_2 generated per g mineral reactant. (b) Measured room temperature pH ($pH_{25°C}$) and calculated in situ pH ($pH_{in\ situ}$). (c) Dissolved SiO_2 concentration. Vertical dashed lines indicate injection of additional fluid into experiment OlivOpx230 at 4514 h. Except where shown, analytical errors are smaller than the symbols. A version of the figure that includes data from Opx230 is provided as Supplemental Fig. S7.

and Fe^{III} in the chrysotile, with the Fe^{III} occupying only the octahedral site (Table 5; Supplemental Fig. S5). The Fe^{III} comprises about 15 mol.% of the total Fe in chrysotile.

Brucite precipitated as large platy crystals up to several hundred microns across and 20 μm thick, with hexagonal terminations evident in many crystals (Fig. 1d). The brucite is typically found immediately adjacent to remnant olivine crystals (e.g., Fig. 1d,e). It is slightly enriched in Fe relative to chrysotile (Mg# = 87), with a nearly homogenous composition throughout the sample as well as within individual crystals (Table 2). Analysis of the brucite by EDS indicated that many crystals contain substantial amounts of Cl (up to 2 wt.%), suggesting that the brucite was intergrown with iowaite [ideal molecular formula $Mg_6Fe^{III}_2Cl_2(OH)_{16}{\cdot}4H_2O$; Braithwaite et al., 1994], similar to observations of this mineral in olivine-only experiments (McCollom et al., 2016). The presence of iowaite intergrown with the brucite was also indicated by Raman analysis (Supplemental Fig. S4). Although Fe^{II} in brucite has Mössbauer parameters that are close to the main doublet observed for the OlivOpx230 sample (Supplemental Fig. S5), the large crystal size precluded the brucite from being included in the fine-grain fraction that was separated from the bulk solids and used for MB analysis (confirmed by SEM). Therefore, the Fe^{II} doublet for this sample included little or no contribution from brucite.

The reacted solids contained 1.52 wt.% magnetite, which occurs as octahedral crystals with diameters ranging from <1 to ~10 μm (Fig. 1d,e). Magnetization analyses at low-temperature (10–300 K) indicated that the magnetite occurs mainly as a cation-substituted magnetite plus a minor amount of pure magnetite (Supplemental Fig. S9). The magnetic behavior is consistent with a few wt.% Ti cation substitution, and is similar to the magnetic results from olivine-only experiments (McCollom et al., 2016). The titanium closure piece of the reaction vessel (Supplemental Fig. S1) is a possible source of Ti in the magnetite.

Carbonate minerals are sparsely distributed throughout the reaction products, some of which were found by EDS to contain only Ca (presumably calcite) while others contained an equal mixture of Mg and Ca (presumably dolomite). Iron was undetectable in the carbonates by EDS. Inspection of the reacted solids by SEM-EDS also revealed the presence of trace amounts of materials with elevated concentrations of Ni plus Fe or of Pt, without detectable O, C, or S. Presumably, these represent metallic phases, including Ni-Fe alloy (possibly awaruite) and native Pt (Supplemental Fig. S8). None of these phases were observed during extensive inspection of the reactant minerals, so they were evidently produced during the experiments.

3.3. Short- and medium-term olivine plus orthopyroxene experiments (OlivOpx230short and OlivOpx230med)

In an effort to examine processes occurring in the early stages of experiment OlivOpx230, a pair of additional experiments were performed to react olivine plus Opx at 230 °C for shorter durations. These experiments lasted 620 h (OlivOpx230short) and 2709 h (OlivOpx230med). The duration of OlivOpx230short was timed to coincide with the earliest phase of OlivOpx230 when little production of H_2 was observed, while OlivOpx230med was intended to examine the period after the initial increase in H_2 production (Fig. 3a). In both of these experiments, however, barely any production of H_2 was observed, with the total amount generated limited to <0.03 mmol g^{-1} (Fig. 3a). These amounts are much less than was observed at comparable times during the early stages of experiment OlivOpx230 (e.g., 0.36 mmol g^{-1} at 840 h and 1.5 mmol g^{-1} at 3351 h). Nevertheless, other aspects of the fluid chemistry in experiments OlivOpx230short and OlivOpx230med were very similar to those observed during the early stages of OlivOpx230, including circumneutral $pH_{25°C}$ and ΣSiO_2 concentrations in the 600–900 μmol kg^{-1} range (Fig. 3a and b; Supplemental Table S1).

Examination of the solid products of both shorter-term experiments by SEM showed that most of the original reactant minerals remained but they were coated with a thin rind of secondary minerals (reaction products for OlivOpx230med are illustrated in Fig. 1g-i and those for OlivOpx230short in Supplemental Fig. S10). The alteration rind had no clear structure at the resolution of the SEM. However, analysis of the secondary products of experiment OlivOpx230med by XRD indicated that they were composed predominantly of serpentine, most likely lizardite, with small amounts of talc (Supplemental Figs. S3 and S11). Results of TGA for OlivOpx230med are shown in Fig. 2b and summarized in Table 4. The TGA results indicate that extent of reaction in OlivOpx230med was very limited, with only 1.9% of the reactants being converted during the experiment.

Owing to the limited abundance of the secondary minerals for both short-term experiments, no magnetic measurements or MB analysis were performed. It also proved impossible to obtain reliable data on their chemical composition with EMPA or EDS. Magnetite was below detection in both experiments. A platy mineral with a hexagonal outline was found sparsely scattered embedded within the alteration rind of both OlivOpx230short and OlivOpx230med (Fig. 1i and Supplemental Fig. S10), which analysis using EDS indicates contains only Fe and O. The composition combined with the shape suggests that this mineral is hematite, although this identification was not confirmed by other methods.

4. DISCUSSION

4.1. Hydrogen production and fluid chemistry in OlivOpx230

The only experiment in this study to generate significant amounts of H_2 and magnetite was OlivOpx230. Production of H_2 during this experiment occurred in three distinct stages (Fig. 4). During the first 1344 h of the experiment (Stage I), only a very small amount of H_2 was generated. At about this time, however, the rate of H_2 production increased and then continued at a steady rate through the measurement at 3359 h (Stage II). Prior to the next measurement at 4488 h, the rate of H_2 production increased

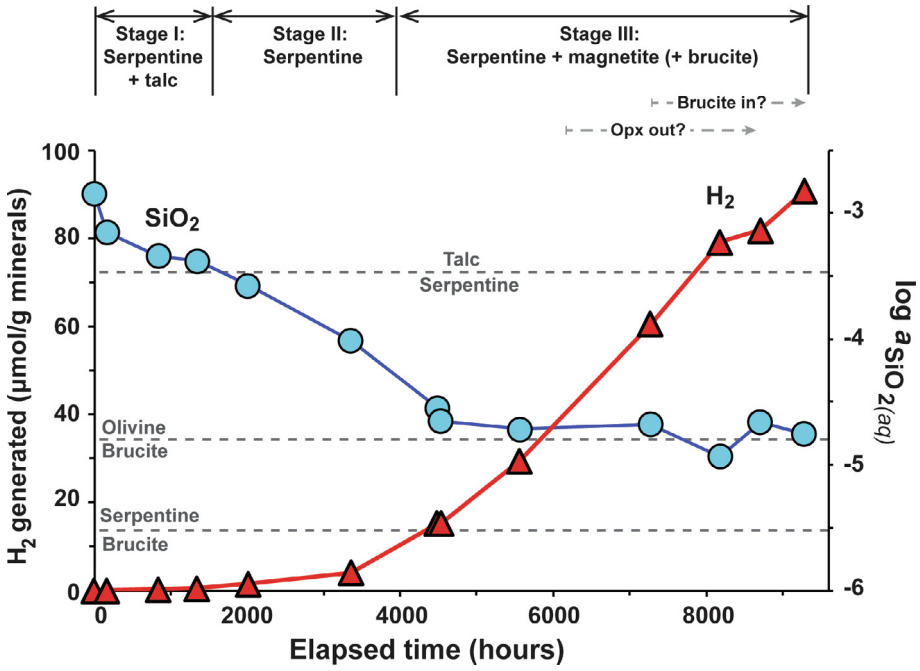

Fig. 4. Production of H_2 and calculated in situ activity of dissolved silica [$a_{SiO2(aq)}$] during experiment OlivOpx230. For reference, the gray dashed lines indicate silica activities for stable equilibrium between talc and serpentine and between serpentine and brucite, as well as for metastable equilibrium between olivine and brucite. The dashed arrows at top right reflect uncertainty over the timing for the disappearance of Opx and for the initiation of precipitation of brucite. For the equilibrium calculations, the observed compositions of the minerals in the OlivOpx230 are used (i.e., $Mg\#_{olivine} = 91$, $Mg\#_{chrysotile} = 90$, $Mg\#_{brucite} = 87$).

even further and then proceeded steadily at this higher rate for the remainder of the experiment (Stage III).

The trends in H_2 production are correlated with changes in dissolved SiO_2 and pH (Figs. 3 and 4). Speciation calculations based on the measured fluid compositions were used to estimate the activity of dissolved $SiO_{2(aq)}$ [$a_{SiO2(aq)}$] during the experiment, and the results are displayed in Fig. 4 as blue circles. Also shown by the horizontal dashed lines in Fig. 4 are silica activities corresponding to equilibrium between talc and serpentine, olivine and brucite, and serpentine and brucite, calculated according to the reactions:

$$0.9Mg_3Si_4O_{10}(OH)_2[talc] + 0.3Fe^{2+} + 1.4H_2O \rightarrow (Mg_{0.9}Fe_{0.1})_3Si_2O_5(OH)_4[serpentine] + 0.6H^+ + 1.6SiO_{2(aq)} \quad (2)$$

$$(Mg_{0.9}Fe_{0.1})_2SiO_4[olivine] + H_2O \rightarrow 2(Mg_{0.9}Fe_{0.1})(OH)_2[brucite] + SiO_{2(aq)} \quad (3)$$

$$(Mg_{0.9}Fe_{0.1})_3Si_2O_5(OH)_4[serpentine] + H_2O \rightarrow 3(Mg_{0.9}Fe_{0.1})(OH)_2[brucite] + 2SiO_{2(aq)}. \quad (4)$$

During stage I, values of $a_{SiO2(aq)}$ converge on the talc-serpentine boundary (Fig. 4), suggesting that metastable equilibrium between these mineral phases was controlling the level of dissolved silica. The presence of these minerals at this stage of OlivOpx230 is likely since both shorter-term experiments produced serpentine (lizardite) accompanied by minor amounts of talc. The limited production of H_2 during Stage I indicates that most of the Fe^{II} released from the dissolving primary minerals was incorporated directly into serpentine and talc with only limited conversion to Fe^{III}. The results of the short-term experiments also indicate that overall reaction rates were relatively slow during this period and production of secondary minerals may have been limited, which would also have contributed to the low H_2 production.

The increase in H_2 production that marks the transition from Stage I to Stage II was accompanied by a decrease in $a_{SiO2(aq)}$, suggesting that the small amount of talc produced early in the experiment had been consumed and was no longer present to buffer the dissolved silica concentration. Precipitation of serpentine likely dominated the secondary mineralogy during Stage II. The increase in H_2 production indicates increased conversion of Fe^{II} to Fe^{III}, which may have been incorporated primarily into serpentine (Seyfried et al., 2007).

The steep increase in H_2 production at the onset of Stage III coincides with a sharp increase in pH from mildly alkaline to strongly alkaline conditions (Fig. 3b). At the same time, the activity of $SiO_{2(aq)}$ leveled off and remained essentially constant for the remainder of the experiment (Fig. 4). The $a_{SiO2(aq)}$ during Stage III converges on values near those calculated for equilibrium between brucite and olivine (Rxn. 3), and remain well above levels expected for equilibrium between serpentine and brucite (discussed further in Section 4.4).

4.2. Reaction path models

Reaction path models were constructed to aid the interpretation of reactions occurring during OlivOpx230. These kinds of models simulate incremental reaction of minerals with an aqueous fluid, and make predictions for the composition of secondary mineral products and the evolution of fluid compositions as the reaction progresses (Bethke, 2008). To facilitate comparison with OlivOpx230, the reactants in the models presented here were assumed to have the same compositions, proportions and fluid:rock ratio as in the experiment. Additional details of the model calculations are provided in Section S3 of the Supplemental Materials.

Three reaction path models were constructed using different relative reaction rates for olivine and pyroxene (note that rates in the context of the models refers to the weight of each mineral dissolved per increment of reaction progress, which doesn't necessarily correlate linearly with elapsed time; see Supplemental Materials). However, reaction path models where olivine reacted at the same rate or faster than Opx failed to reproduce critical aspects of the experimental observations, so results for these models are presented only in the Supplemental Materials (see Supplemental Figs. S12 and S13). For instance, these models fail to predict the absence of Opx in the solids remaining at termination of the experiments, but instead predict that

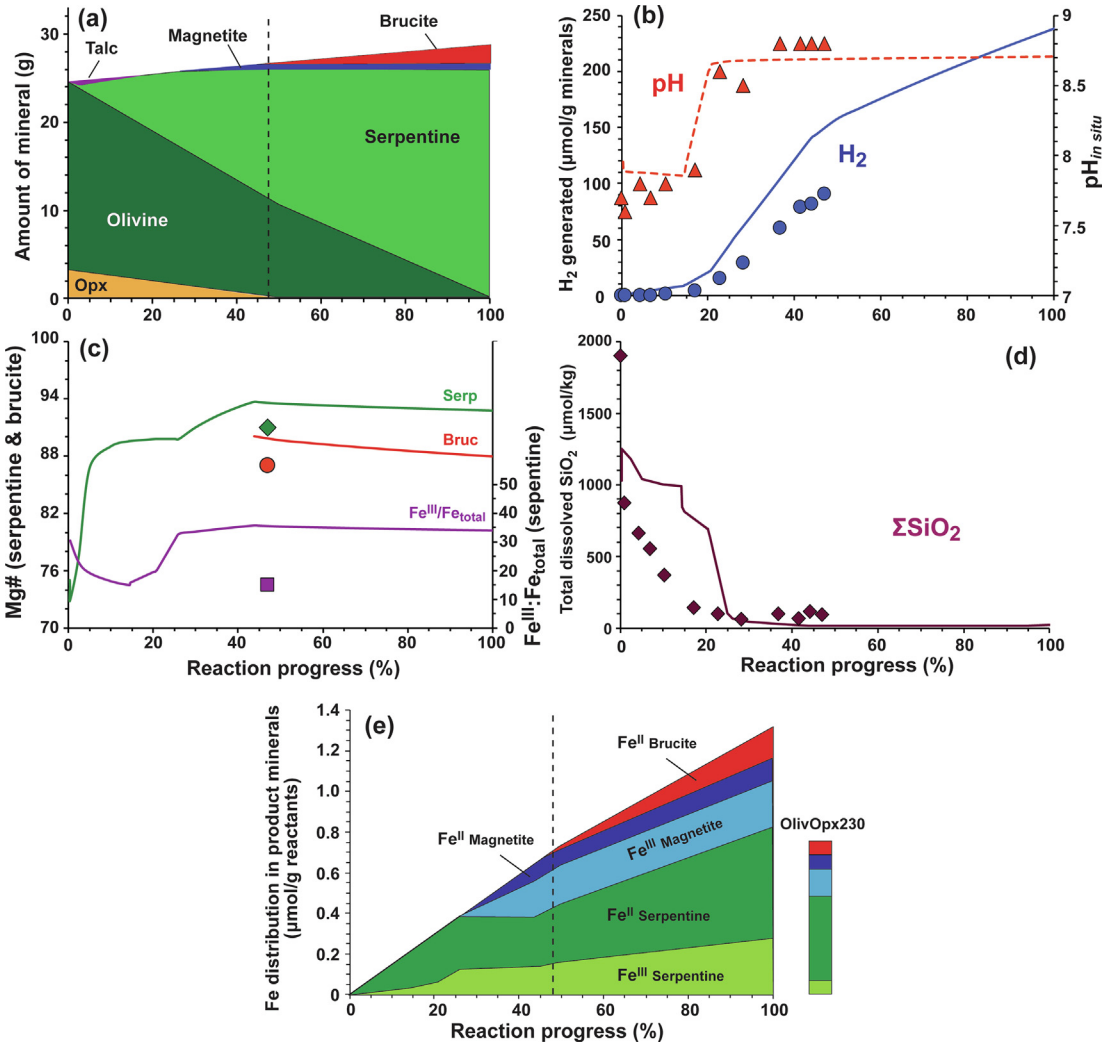

Fig. 5. Results of reaction path model to simulate reaction of the olivine-Opx mixture in experiment OlivOpx230 at 230 °C. For this model, Opx was allowed to react at a rate two times faster than olivine. Results of experiment OlivOpx230 are shown for comparison (symbols). (a) Composition of solids as the reaction progresses, including reactants and secondary products. Trace amounts of tremolite are also predicted to precipitate during the early stages of the reaction path and is later replaced by calcite; however, the amounts of these minerals are too small to be visible in the diagram. The dashed vertical line indicates the approximate degree of reaction progress in OlivOpx230. Note that because Opx is constrained to react more rapidly than olivine, the 53 wt.% of reactant minerals consumed in the experiment corresponds to ~47% reaction progress in the model. (b) Predicted in situ pH and amount of H_2 generated. (c) Predicted Mg# of chrysotile and brucite, and the Fe^{III}:Fe_{total} ratio of chrysotile. (d) Concentration of total dissolved SiO_2. (e) Partitioning of Fe among reaction products in the model, with the partitioning observed for products of OlivOpx230 shown by the bar on the right (see Supplemental Table S4for calculations).

substantial Opx should have remained when the experiment was terminated. These models also predict that magnetite and brucite would begin to precipitate at an earlier stage of reaction progress than is indicated by the experimental results.

The absence of Opx in the solids remaining at the termination of OlivOpx230 requires that it reacted at least two times more rapidly than olivine during the experiment (i.e., each grain of Opx reacted at least twice as fast as an equivalent olivine grain). Accordingly, Fig. 5 shows a reaction path model where Opx is allowed to react two times faster than olivine. Selected experimental results from OlivOpx230 are also shown in the figure for comparison with the model. To display this data on the diagrams, it is assumed for simplicity that reaction progress during OlivOpx230 was a linear function of time. However, if the net conversion rates of the reactant minerals varied as a function of time during the experiment (for instance, when the pH increased), then the horizontal position (i.e., *x*-axis value) of the experimental data points may not accurately represent the extent of reaction achieved at any given sample point (see Supplemental Materials).

In the earliest segment of the reaction path shown in Fig. 5, chrysotile and talc precipitate along with small amounts of tremolite as the reactant minerals begin to dissolve. With continued reaction, the talc and tremolite redissolve, and the predicted secondary mineral assemblage becomes dominated by serpentine. During this interval, H_2 is generated only from Fe^{III} incorporated into serpentine. The disappearance of tremolite is accompanied by a steep rise in pH and precipitation of trace amounts of calcite, which then remains through the end of the predicted reaction path. In the model, the pH change is driven by the conversion of tremolite to calcite, which can be expressed in simplified terms as:

$$\begin{aligned} &3Ca_2Mg_5Si_8O_{22}(OH)_2[\text{tremolite}] \\ &\quad + 42Mg_2SiO_4[\text{olivine}] + 63H_2O + 6HCO_3^- \\ &\quad \rightarrow 33Mg_3Si_2O_5(OH)_4[\text{serpentine}] \\ &\qquad + 6CaCO_3[\text{calcite}] + 6OH^- \end{aligned} \quad (5)$$

although the reaction would have involved Fe-bearing components as well. In the reaction, the Mg and Si released from tremolite combine with components from olivine to precipitate as serpentine.

Following the pH increase, magnetite joins the product mineral assemblage, and H_2 is generated from precipitation of both magnetite and Fe^{III}-bearing serpentine. When Opx eventually becomes depleted at 50% reaction progress, brucite joins serpentine as the predominant secondary products that precipitate during each additional increment of reaction progress. Only small amounts of magnetite are added to the secondary minerals during the last half of the predicted reaction path, so that H_2 production during the latter stage of the reaction is once again dominated by partitioning of Fe^{III} into serpentine.

The model shown in Fig. 5 reproduces many key features of OlivOpx230. These features include a transition from mildly to strongly alkaline pH after the reaction had proceeded for some time, a lag period prior to onset of significant H_2 production, and amounts of H_2 generation as a function of reaction progress that are similar to those observed during the experiment (Fig. 5b). The model also predicts ΣSiO_2 concentrations that are initially high and then drop to very low levels as the reaction progresses (Fig. 5d). Solid solution compositions for serpentine and brucite predicted by the models are similar to those observed in the experiment, although the model predicts somewhat lower Fe contents (higher Mg#) than observed (Fig. 5c). For 53% conversion of the reactants, the model predicts that the solids should contain ~1.9 wt.% magnetite, in reasonably good agreement with the experimental value of 1.52 wt.%.

While the reaction path provides a close match to many aspects of OlivOpx230, it is worth noting some discrepancies between the model predictions and experimental observations. For instance, the reaction path model predicts greater generation of H_2 per unit of rock reacted than is observed in the experiment, by a factor of ~1.6. In large part, this difference is attributable to the much higher Fe^{III}:Fe_{total} ratio predicted for serpentine in the model (~0.35) than is observed in the experiment (~0.15; Fig. 5c), suggesting that the solid-solution model for serpentine used in the model may need to be modified. The models also predict ΣSiO_2 concentrations during the latter stages of reaction progress that are substantially lower than those observed in the experiments (Fig. 5d). A possible explanation for this discrepancy is discussed in a subsequent section.

4.3. Interpretation of reaction pathway in OlivOpx230

Overall, the reaction path model shown in Fig. 5 provides a good match to the results of OlivOpx230, and support the following interpretation of the evolution of secondary mineralogy and fluid chemistry during OlivOpx230. During Stage I, dissolution of the reactants led to precipitation of a combination of serpentine and talc, as observed in the shorter term experiments. Dissolution of the trace amounts of quartz and other contaminants present in the starting Opx most likely contributed additional SiO_2 to the system that enhanced precipitation of talc. The relatively high $aSiO_{2(aq)}$ during this stage reflects dissolution of Si-rich phases and buffering by the talc-serpentine assemblage (Fig. 4). Dissolution of trace amounts of Cpx or plagioclase may also have resulted in precipitation of small amounts of tremolite or some other Ca-bearing secondary phase during this interval.

Although Opx evidently dissolved more rapidly than olivine on a gram-per-gram basis during the experiment, the greater overall mass of olivine means it still contributed a greater flux of elements to the solution than Opx. As a consequence, the talc formed early in the experiment dissolved with continued reaction and the $aSiO_{2(aq)}$ dropped below the talc-serpentine equilibrium level, marking the transition to Stage II. During this stage, serpentine evidently dominated the reaction products and minor amounts of H_2 were generated primarily by incorporation of Fe^{III} into the serpentine. Based on the model results, precipitation of significant magnetite probably did not begin until later in the experiment.

Following conversion of ~20 wt.% of the reactant minerals (≈18% reaction progress), the pH abruptly increased from mildly alkaline ($pH_{in\ situ} = 7.9$) to more strongly alkaline ($pH_{in\ situ} = 8.6$) conditions, apparently driven by Rxn. 5 or an analogous reaction (Fig. 3). The increase in pH marks the beginning of Stage III, and corresponds with a steep increase in the rate of H_2 generation that continued throughout this stage (Fig. 4). Based on the model results, the increase in H_2 generation per increment of reaction progress coincided with the onset of magnetite precipitation, which then continued throughout the stage. The steady rate of H_2 production during Stage III indicates that the stoichiometry of the reaction remained essentially constant during this interval, with constant rates of reactant dissolution and product precipitation. Similar constant reaction stoichiometries and steady rates of magnetite production over long intervals have also been reported in previous experimental studies of serpentinization (Malvoisin et al., 2012a; McCollom et al., 2016). The model predicts that the proportion of Fe partitioned into serpentine should decrease in the interval following the pH increase, resulting in higher Mg# (Fig. 5c). However, it is unclear whether this occurred during OlivOpx230, since there was no detectable spatial variation in the chemical composition of serpentine in the products.

Because the solids were not available for inspection prior to termination, it is not possible to determine precisely when Opx became exhausted or when brucite began to precipitate in the experiment. It appears likely, however, that a considerable amount of Opx still remained at the onset of Stage III, when significant production of magnetite and H_2 was initiated (Fig. 5a). The amount of Opx would have continued to decrease during Stage III, eventually disappearing completely at some point prior to termination.

According to the model predictions, precipitation of brucite should begin only when Opx is nearly exhausted (Fig. 5a). As a consequence, brucite probably only began to precipitate towards the end of the OlivOpx230, well after it had entered Stage III. A late onset would be consistent with the limited amount of brucite present in the reacted solids and its close spatial association with olivine, since a more widespread distribution of brucite would be expected if it had precipitated throughout Stage III. The models also predict that the rate of H_2 generation should decrease slightly after the onset of brucite precipitation (Fig. 5b). An intriguing possibility, though one that cannot be verified at this time, is that the slight inflection in H_2 production observed in the experiment between 8183 h and 8711 h (Fig. 3a) marked the transition point for depletion of Opx and onset of brucite precipitation. If this is the case, the experiment may have actually entered a fourth stage just prior to termination of the experiment where H_2 production began to be dominated by precipitation of serpentine plus brucite rather than serpentine plus magnetite (Fig. 5).

The model predicts that if OlivOpx230 had been allowed to continue, further precipitation of secondary products would have become dominated by serpentine and brucite with little additional magnetite. Production of H_2 would have continued during this final stage of the reaction, but the amount generated per increment of reaction progress would have decreased slightly. Nevertheless, the model predicts that if the reaction had gone to completion the amount of H_2 generated would have increased by an additional 50% above the amount produced during the experiment.

4.4. Controls on silica activity

One of the key outcomes of OlivOpx230 is that ΣSiO_2 concentrations were essentially constant throughout the second half of the experiment at levels well above those expected for serpentine-brucite equilibrium (Fig. 4). Additional insight into the factors that regulated ΣSiO_2 concentrations during this experiment can be obtained from activity-activity diagrams that depict the stabilities of minerals. The diagram in Fig. 6a shows calculated $a_{SiO2(aq)}$ and $pH_{in\ situ}$ of the fluids during the 230 °C experiments projected onto mineral stability fields for the system Mg-Ca-Fe-Si-C-O-H. Also shown in the figure for reference are fluid compositions from two previous experiments performed at the same temperature that used olivine as the only solid reactant (McCollom et al., 2016). For the diagrams, the solid-solution compositions for serpentine and brucite that were observed in OlivOpx230 are used to constrain the stability limits of these minerals.

The dashed blue line in Fig. 6a represents the predicted trajectory of the fluid composition for the reaction path model in Fig. 5. The predicted path initially converges on the invariant point for talc, tremolite, and serpentine, reflecting fluid buffering by this assemblage in the early stages of the reaction. The fluid then traverses the serpentine stability field during a short interval of reaction progress (Fig. 5d) and converges on the serpentine-brucite boundary, as indicated by the blue cross (note that the reaction path does not converge exactly on the serpentine-brucite boundary in Fig. 6a because the model predicts somewhat different compositions for these solid-solutions than are represented in the diagram or observed in the experiments; see Fig. 5c).

The red triangles in Fig. 6a indicate fluid compositions during experiment OlivOpx230. The first fluid sample for this experiment lies at the talc-tremolite boundary and, as the reaction progresses, fluid compositions first converge on the talc-serpentine boundary and then continue into the serpentine stability field. During the first half of the experiment, the $a_{SiO2(aq)}$ gradually decreases but remains within the serpentine field, likely reflecting precipitation of chrysotile and a decreasing contribution of Opx relative to olivine to the dissolved SiO_2 as the reaction progressed. Fluid compositions during the second half of the experiment maintained nearly constant $aSiO_{2(aq)}$, but remained well within the serpentine field despite the presence of both brucite and dolomite at the end of the experiment (Fig. 6a). The persistence of fluid compositions within the serpentine field and far from the boundaries for brucite and dolomite requires that chrysotile did not attain equilibrium with either mineral, even though both were present when the experiment was terminated. For equilibrium to be achieved, either brucite or dolomite would have had to react with

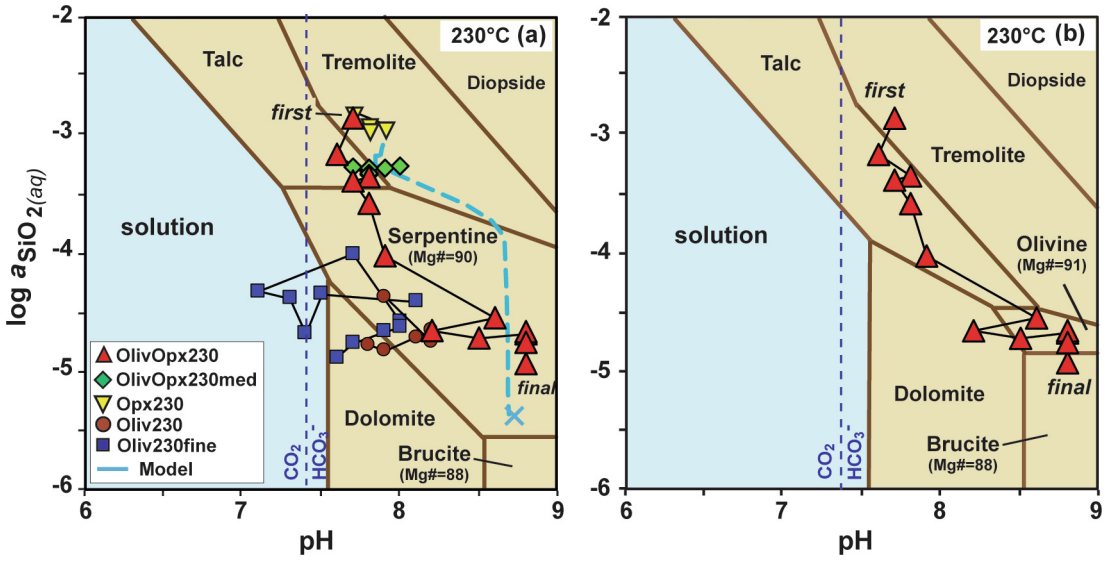

Fig. 6. Calculated in situ fluid compositions for laboratory experiments at 230 °C projected onto mineral stability diagrams for Mg-bearing minerals in the Mg-Fe-Ca-Si-O-C-H system as a function of pH and activity of dissolved silica. Panel (a) shows stable equilibrium mineral assemblages for the system, while panel (b) shows metastable assemblages calculated by excluding serpentine. Compositions of serpentine and brucite are constrained to approximate those observed in the experiments. The dashed light blue line in (a) traces the predicted fluid composition during the reaction path model shown in Fig. 5. Dashed dark blue lines separate predominance fields for $CO_{2(aq)}$ and HCO_3^- among dissolved carbon species. For construction of the diagrams, concentration of dissolved Mg, Ca, Na, Cl, and H_2 are set to the values in the final samples of the experiments, while dissolved Fe was assumed to in equilibrium with magnetite since it was below detection. Results for Oliv230 and Oliv230fine in (a) are from McCollom et al. (2016). (For interpretation of the references to color in this figure legend, the reader is referred to the web version of this article.)

SiO_2 to form chrysotile, which would have lowered ΣSiO_2 concentrations by nearly an order of magnitude below those observed in the experiment (see also Fig. 4).

The maintenance of $aSiO_{2(aq)}$ at constant levels well above the serpentine-brucite boundary suggests that some other reaction regulated the activity of silica during the second half of the experiment. Fig. 6b shows a mineral stability diagram where serpentine has been excluded from participating in equilibrium with the fluid and other mineral phases. In this diagram, it can be seen that the fluid compositions appear to converge on $aSiO_{2(aq)}$ and pH levels that are close to the metastable invariant point for the olivine-brucite-dolomite assemblage (note that equilibration of this mineral assemblage would be metastable since olivine is thermodynamically unstable relative to serpentine at the experimental conditions). Convergence of $a_{SiO2(aq)}$ at levels consistent with the olivine-brucite metastable boundary was also observed in experiments performed with olivine as the only solid reactant under the same conditions (Fig. 6a; McCollom et al., 2016).

One possible explanation for these observations is that silica activities in the experiments are being regulated by reactions occurring at the surface of dissolving olivine. Dissolution of olivine at acidic to circumneutral pH produces a thin layer (~a few unit-cells thick) on the mineral surface that is enriched in Si and depleted in Mg (e.g., Pokrovsky and Schott, 2000; Oelkers et al., 2018). At alkaline pH, however, the dissolution mechanism shifts and a Si-depleted, Mg-enriched surface layer develops. The structure of this thin Mg-rich layer apparently resembles individual sheets of brucite, and the rate-limiting step for olivine dissolution at higher pH is thought to involve hydrolysis and detachment of Mg^{+2} ions from this Si-depleted layer (Pokrovsky and Schott, 2000; Oelkers et al., 2018).

This suggests the possibility that exchange of SiO_2 between the fluid and the surface of dissolving olivine may have regulated ΣSiO_2 concentrations during the experiments. The exchange can be represented by the general reaction:

$$Mg_2SiO_4[\text{olivine}] + 2H_2O \rightleftharpoons 2Mg(OH)_2[\text{surface}] + SiO_{2(aq)} \quad (6)$$

where $Mg(OH)_2$ [surface] represents the Si-depleted surface layer (for simplicity, the reaction is written only for the Mg endmembers although Fe would also be present in the olivine and surface layer). If this reaction is sufficiently rapid and reversible, local equilibrium could be established. Since the surface layer has a brucite-like structure, equilibration of this reaction might be expected to regulate $a_{SiO2(aq)}$ at levels close to the metastable olivine-brucite equilibrium boundary. This mechanism might therefore explain why $aSiO_{2(aq)}$ maintained levels near olivine-brucite equilibrium for extended periods of time during OlivOpx230 and in the olivine-only experiments.

It should be emphasized that equilibration of Rxn. 6 would not inhibit the continued dissolution of olivine or halt reaction progress during serpentinization. As Mg^{+2} ions are removed from the surface layer and precipitate as serpentine or brucite, the interface between the surface layer and pristine olivine would continuously migrate further

into the olivine crystals. As long as Rxn. 6 equilibrates at a faster rate than Mg^{+2} ions are removed from the Si-depleted surface layer, the exchange reaction would be able to regulate the silica activity. Indeed, as suggested by olivine dissolution studies, the rate at which Mg^{+2} ions are removed from the surface layer may ultimately be the rate limiting step for dissolution of olivine during the serpentinization experiments.

Regulation of $a_{SiO2(aq)}$ by Rxn. 6 would also require that it proceeds more rapidly than the reaction of dissolved SiO_2 with brucite to form serpentine. That is, if conversion of brucite to serpentine proceeded more rapidly than Rxn. 6, the $a_{SiO2(aq)}$ would be expected to decrease to the serpentine-brucite equilibrium boundary, which was not observed in either OlivOpx230 or the previous olivine-only experiments (Fig. 6a). Other experimental results suggest that the reaction of SiO_2 with brucite can be relatively sluggish under hydrothermal conditions (Tutolo et al., 2018), which may have precluded brucite from equilibrating with serpentine under the conditions of the experiments. Nevertheless, lower ΣSiO_2 concentrations consistent with serpentine-brucite equilibrium have been observed in some laboratory serpentinization studies (e.g., Okamoto et al., 2011; Ogasawara et al., 2013; Grozeva et al., 2017), implying that reactions involving brucite and serpentine may be sufficiently rapid under some experimental conditions to regulate $a_{SiO2(aq)}$.

4.5. Relative reaction rates and effect of pH on overall rate

The present results do not provide sufficient information to evaluate absolute rates of reaction for olivine and Opx at the experimental conditions. However, they do allow some general observations concerning rates to be made. The results of OlivOx230 indicate that Opx reacted more rapidly than olivine on a gram-per-gram basis, probably by a factor of about two. The outcome of Opx230 (which contained only Opx) would appear to be generally consistent with this result, since Opx in that experiment was found to react about five times more rapidly than was previously observed for olivine alone at the same conditions and initial grain size (Table 4; McCollom et al., 2016).

These findings are in agreement with some previous experimental studies, but disagree with others. For instance, in studies using individual minerals as reactants, Martin and Fyfe (1970) found that forsterite reacted more rapidly than enstatite below ~320 °C, and Ogasawara et al. (2013) similarly reported that olivine reacted about five times more rapidly than Opx at 250 °C. Olivine also dissolves more rapidly than pyroxenes in laboratory dissolution experiments (e.g., Pokrovsky and Schott, 2000; Oelkers and Schott, 2001). Thus, several previous studies performed with individual mineral reactants suggest that olivine should react more rapidly than Opx during serpentinization, contrary to the observations from OlivOpx230 and Opx230. In experiments where both olivine and Opx were included as reactants, some studies have reported that olivine reacted more rapidly than Opx (e.g., Marcaillou et al., 2011; Huang et al., 2017a) while others found that Opx reacted more rapidly than olivine as was observed in OlivOpx230 (e.g. Klein et al., 2015; Grozeva et al., 2017; Klein and Le Roux, 2020).

Together, these results suggest that the relative reaction rates of olivine and Opx may be variable depending on environmental conditions within the experiments. However, because the experimental protocols employed in these studies encompass a wide of environmental conditions (temperature, reactant composition, grain size, pH, fluid composition, etc.), it is not immediately clear which factors the relative rates are most sensitive to. Consequently, more study is needed to understand why Opx evidently reacts more rapidly than olivine under some circumstances and more slowly under others.

The results from OlivOpx230 also reflect a strong dependence of serpentinization rates on pH as reported by McCollom et al. (2020). In the current study, the extent of reaction in OlivOpx230 (53%) was found to be far greater than that in OlivOpx230med (1.9%). A likely explanation for this difference is that the reaction rate during the early stages of OlivOpx230 was relatively slow and similar to the rate in OlivOpx230med, but that the overall reaction rate accelerated sharply when OlivOpx230 transitioned to strongly alkaline pH (i.e., at the onset of Stage III). This interpretation is supported by the experimental results of McCollom et al. (2020), which showed steep increases in

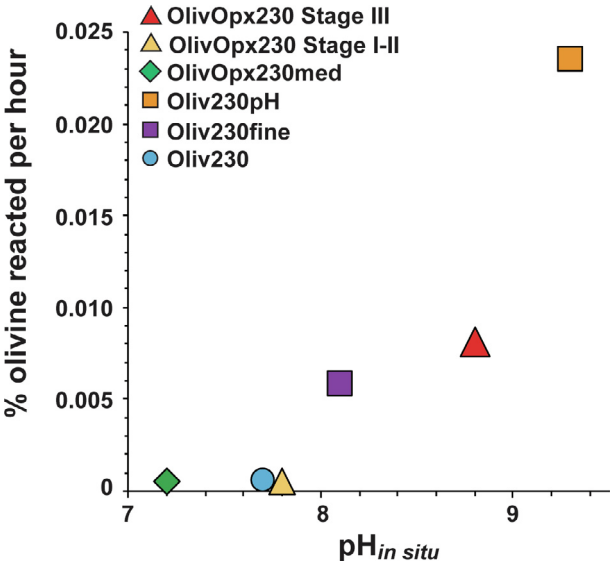

Fig. 7. Reaction rate of olivine in laboratory serpentinization experiments conducted at 230 °C as a function of in situ pH. Experiments Oliv230, Oliv230fine, and Oliv230pH included olivine as the only solid reactant. For OlivOpx230, estimated reaction rates are shown separately for Stages I-II (up to 4000 h reaction) and for Stage III following the increase in pH (4000–9287 h). For Stages I-II, it is assumed that olivine reacts at a rate similar to that in OlivOpx230med and Oliv230, while the value for Stage III is calculated based on the final extent of olivine reaction indicated by the TGA results (45%) after subtracting the estimated amount reacted during Stages I-II (2.1%; see Supplemental Table S5 for calculation). The initial grain size is < 53 μm for Oliv230fine and Oliv230pH, and 53–212 μm for other experiments. Data for olivine-only experiments are from McCollom et al. (2016, 2020).

reaction rates at strongly alkaline pH relative to those under mildly alkaline conditions both for olivine alone and for an olivine-Opx mixture. In particular, the results of experiment OlivOpx230pH from McCollom et al. (2020) showed a steep increase in both H_2 generation and overall reaction rate when the pH was externally manipulated to transition from mildly alkaline to strongly alkaline conditions, mirroring the observations from OlivOpx230 (see Fig. 6 in McCollom et al., 2020, for a direct comparison of these experiments).

Whether the transition to strongly alkaline pH in OlivOpx230 accelerated the reaction rates of olivine and Opx equally remains to be determined. Notably, however, the inferred rate of reaction for the olivine component of OlivOpx230 appears to be consistent with rates observed in olivine-only experiments as a function of pH at the same temperature (Fig. 7; Supplemental Table S5). This suggests that fluid pH is the main driver for the increased rate of olivine reaction in OlivOpx230, as opposed to any change in the local chemical environment caused by the presence of Opx. Previously, Huang et al. (2017a) reported that the presence of Opx stimulated more rapid reaction of olivine in laboratory experiments at 311 °C, which they attributed to the effects of dissolved Al and Cr derived from Opx on the reactivity of olivine. However, the results of OlivOpx230 show no evidence that transfer of dissolved elements from Opx stimulated reaction of olivine (or vice versa), but instead point to pH as the primary factor responsible for the increase in reaction rate.

4.6. Partitioning of Fe among products

The rate and total amount of H_2 generated during serpentinization are intimately linked to how Fe is partitioned among the products as the reaction proceeds (Rxn. 1). Over the years, many different factors have been proposed to influence how Fe gets partitioned among the products, including the Fe content and relative proportions of precursor minerals, the prevailing activity of silica, temperature, fluid pH, the evolving oxidation state of the system, which polymorph of serpentine precipitates, kinetics of component reactions, thermodynamic equilibrium among reaction products, extent of reaction progress, and dissolved CO_2 concentration (e.g., Moody, 1976b; Evans and Trommsdorf, 1972; Janecky and Seyfried, 1986; Frost and Beard, 2007; Seyfried et al., 2007; Evans, 2008; McCollom and Bach, 2009; Marcaillou et al., 2011; Klein et al., 2013; McCollom et al., 2016, 2020; Syverson et al., 2017; Ueda et al., 2017; Huang et al., 2017b; Tutolo et al., 2018; Mayhew and Ellison, 2020). Thus far, however, there appears to be little consensus about which of these factors is most dominant under a given set of circumstances. The results of this investigation and comparison with other experimental studies allows some of these ideas to be further evaluated.

Detailed information on the distribution of Fe among reaction products has only rarely been reported in laboratory serpentinization studies, but the data that are currently available are summarized in Fig. 8 along with the results from this study. The serpentine from OlivOpx230 and Opx230 are seen to have Mg# values close to those of the original olivine and Opx reactants (Fig. 8a), with significantly lower Mg# (i.e., higher Fe content) than other laboratory serpentinization experiments (Fig. 8a). The Fe^{III}: Fe_{total} ratio of serpentine from OlivOpx230 is similar to that from several olivine-only experiments, but is substantially lower than ratios observed in other studies including lherzolite experiments, olivine-only experiments conducted at $pH_{25°C} > 11$, and Opx230 (Fig. 8c). Brucite from OlivOpx230 has Fe contents intermediate between the relatively low Fe contents of brucite precipitated in most olivine-only experiments and the Fe-enriched brucite formed in high-pH olivine experiments and the lherzolite experiment of Seyfried et al. (Fig. 8b). The amount of magnetite generated as a function of reaction progress in OlivOpx230 is similar to that observed during reaction of olivine-only at high pH and in the lherzolite experiment of Marcaillou et al. (2011), but substantially less than observed in other olivine-only experiments (Fig. 8d).

In general, the experiments shown in Fig. 8 that attained more strongly alkaline pH ($pH_{25°C} > 11$), including OlivOpx230, the lherzolite experiment of Seyfried et al. (2007) and the olivine-only experiments shown by the orange circles, exhibit higher Fe contents for serpentine and brucite and lower magnetite production than other experiments with lower pH [note that the lherzolite experiment of Marcaillou et al. (2011) at 300 °C had a mildly acidic $pH_{25°C} = 5.1–5.8$]. This may indicate that higher pH favors greater partitioning of Fe into serpentine and brucite and less into magnetite (McCollom et al., 2020). However, additional factors such as bulk reactant composition, extent of reaction, and thermodynamics may have also contributed to this trend, so further study is required to confirm a pH effect and identify the underlying mechanism.

A closer comparison of the results of OlivOpx230 with the lherzolite experiment of Seyfried et al. (2007) allows for critical evaluation of additional factors that have been hypothesized to regulate the partitioning of Fe and production of H_2 during serpentinization. As seen in Fig. 9, the fluid composition in these two experiments evolve along similar trajectories as the reactions progress. In both cases, there was essentially no H_2 production early in the experiment followed by a steep increase in H_2 concurrent with a increase in pH to strongly alkaline conditions. A steep decrease in ΣSiO_2 concentration also accompanies the increase in H_2 production in both experiments (from 430 μmol kg^{-1} to below detection in Seyfried et al., 2007; Fig. 4).

Despite these similarities in fluid compositions, the reaction pathways that were responsible for generation of H_2 in the two experiments were very different. While the reaction products from OlivOpx230 included abundant magnetite (1.52 wt.%) along with chrysotile and brucite, reaction of lherzolite in the Seyfried et al. experiment produced only chrysotile and brucite with very little or no magnetite (<0.014 wt.%). The proportion of Fe in chrysotile serpentine was similar in both experiments (Fig. 8a), but brucite produced in the lherzolite experiment had a much higher Fe content (Fig. 8b). In addition, the chrysotile from the lherzolite experiment contained a much higher proportion

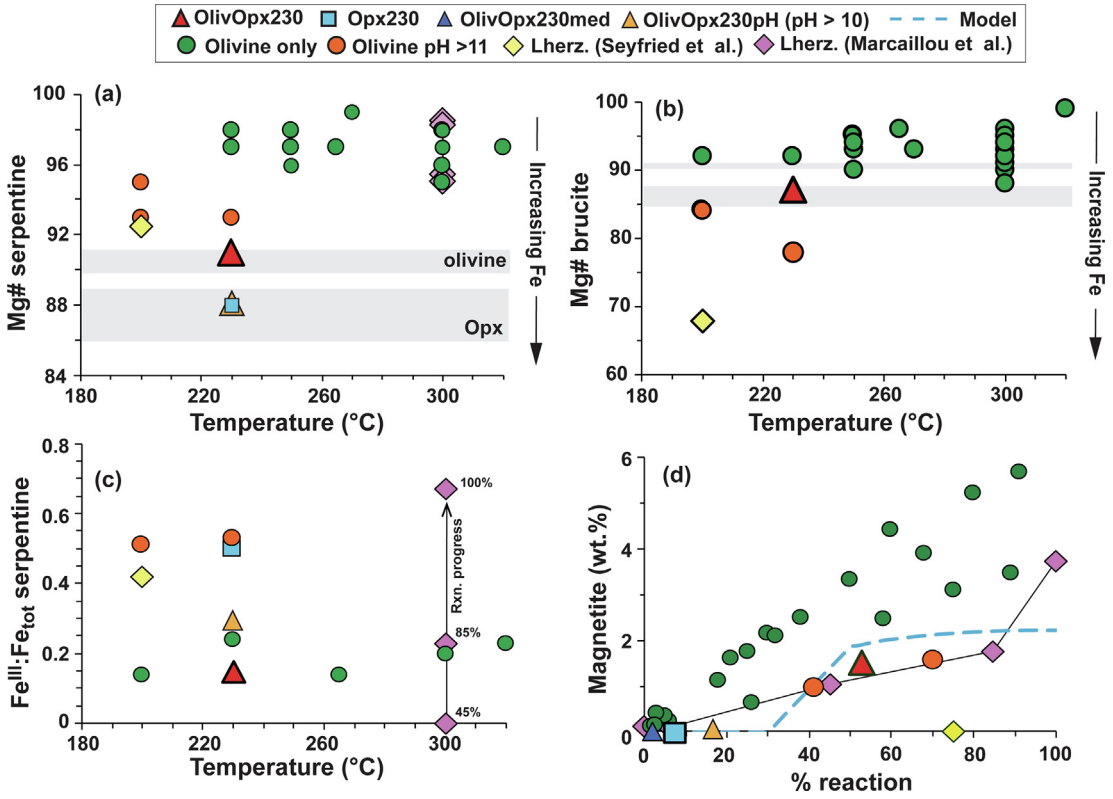

Fig. 8. Distribution of Fe among reaction products in serpentinization experiments. Panels show compositions of (a) serpentine and (b) brucite produced during laboratory serpentinization experiments, (c) proportion of ferric Fe (Fe^{III}) in the total Fe (Fe_{tot}) for serpentine, and (d) magnetite produced as a function of extent of reaction. Experiments using olivine as the only solid reactant are represented by circles, with those experiments conducted at $pH_{25°C} > 11$ plotted separately as orange circles (Lafay et al., 2012; McCollom et al., 2020). Experiments performed with lherzolitic compositions are shown as diamonds. Results for OlivOpx230pH are from an experiment containing both olivine and Opx at the same proportions and initial grain size as in OlivOpx230, but where the $pH_{25°C}$ was manipulated to attain values above 10 part way through the experiment (McCollom et al., 2020). Data for the lherzolite experiment of Marcaillou et al. (2011) reflect changes in Fe distribution with increasing reaction progress, with percent reaction shown in (c). The gray boxes in (a) and (b) outline the range of compositions for olivine and Opx reactants used in the experiments. In (d), the dashed blue line corresponds to the reaction path model shown in Fig. 5. Data sources for olivine experiments: Okamoto et al. (2011), Malvoisin et al. (2012a,b), Lafay et al. (2012), Ogasawara et al. (2013), McCollom et al. (2016, 2020), and Ueda et al. (2017). Data sources for lherzolite experiments: Seyfried et al. (2007) and Marcaillou et al. (2011). The extent of reaction for the lherzolite experiment of Seyfried et al. (2007) is estimated at ~75% based on the description of reaction products provided in that study. (For interpretation of the references to color in this figure legend, the reader is referred to the web version of this article.)

of Fe^{III} than that in OlivOpx230 (Fig. 8c). As a consequence of these differences, most of the H_2 generated in OlivOpx230 (~67%) is associated with precipitation of magnetite (Supplemental Table S3), while H_2 in the lherzolite experiment resulted almost entirely from precipitation of Fe^{III}-bearing serpentine.

Seyfried et al. (2007) proposed that the high pH and strongly reducing conditions (i.e., high H_2 levels) of their lherzolite experiment may have favored partitioning of Fe into serpentine and brucite rather than magnetite. However, the pH and dissolved H_2 concentrations in OlivOpx230 were similar to those of the lherzolite experiment (Fig. 9), and partitioning of Fe into magnetite was not inhibited. Experimental serpentinization of olivine at high pH in the study of McCollom et al. (2020) also produced substantial amounts of magnetite despite elevated H_2 concentrations. Furthermore, the proportion of Fe partitioned into magnetite during experimental serpentinization of olivine does not decrease as the reactions progress and H_2 accumulates, as would be expected if more strongly reducing conditions inhibited magnetite formation (Fig. 8d; Malvoisin et al., 2012a; McCollom et al., 2016). Thus, it appears unlikely that either high pH or a strongly reducing environment can fully account for preferential partitioning of Fe into chrysotile and brucite or the absence of magnetite in the lherzolite experiment, although both factors may contribute.

Alternatively, Seyfried et al. (2007) proposed that reaction kinetics may have favored partitioning of Fe^{III} into serpentine rather than magnetite. That is, if precipitation of serpentine proceeds more rapidly than precipitation of magnetite, then rapid uptake of the Fe released from dissolution of the primary reactants into serpentine might preclude magnetite formation. If this were the case, however,

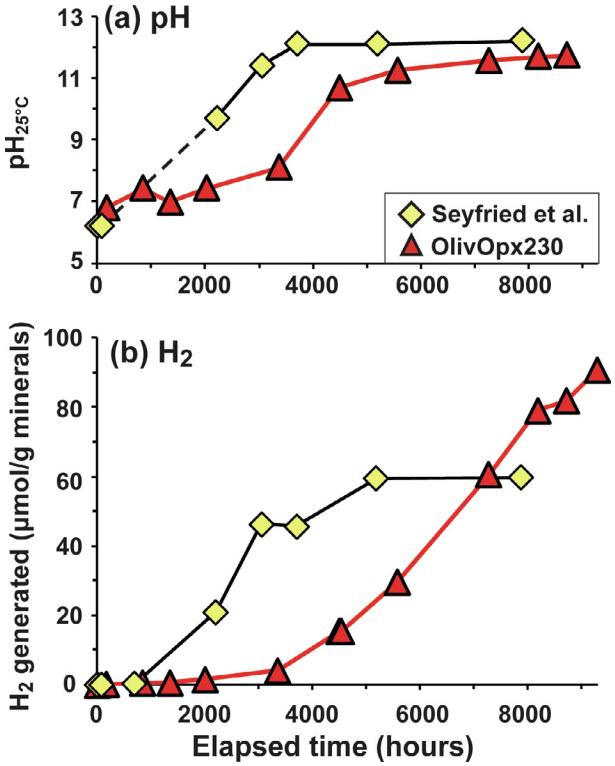

Fig. 9. (a) Room-temperature pH and (b) generation of H_2 during OlivOpx230 compared with results of Seyfried et al. (2007) for experimental serpentinization of lherzolite at 200 °C. No pH measurements were obtained between 75 h and 2209 h in the Seyfried et al. (2007) experiment. For the Seyfried et al. (2007) experiment, the amount of H_2 generated was estimated from the measured fluid concentrations and estimates of the amount of fluid remaining in the reaction cell prior to each sample.

rapid serpentine precipitation and inhibition of magnetite formation would have been expected in OlivOpx230 as well, given the similar temperatures and fluid compositions. Since magnetite was not precluded from forming in OlivOpx230 (or in other experiments with similar temperatures and fluid chemistries; McCollom et al., 2020), it seems unlikely that rapid precipitation of serpentine can explain the absence of magnetite in the lherzolite experiment.

Another possible alternative explanation is that the differences in Fe partitioning between these two experiments is attributable to thermodynamic factors. As seen in Fig. 5, the equilibrium reaction path model provides a fairly close match to the results of OlivOpx230 both for the overall abundance of secondary products and for the distribution of Fe among them (Fig. 5e). The overall agreement between the model and experimental results suggests that thermodynamic equilibrium was a dominant factor controlling the partitioning of Fe among the reaction products during OlivOpx230. Thermodynamic models predict that decreasing temperatures and higher Opx:olivine ratios in the reactants favor increased partitioning of Fe into serpentine and brucite relative to magnetite at equilibrium (Klein et al., 2013: see Supplemental Fig. S14), and also predict that magnetite should not precipitate at 200 °C for lherzolitic compositions like that used by Seyfried et al. (2007). Thus, both the absence of magnetite and relatively high Fe contents for serpentine and brucite in the Seyfried et al. (2007) experiment are also generally consistent with thermodynamic models, albeit the models do predict somewhat lower Fe^{III}: Fe_{total} ratio for serpentine and lower Fe contents for brucite than were observed in their experiment (Klein et al., 2013).

Syverson et al. (2017) also observed a higher rate of H_2 generation following an increase in pH during serpentinization of an olivine-talc mixture at 300 °C. Those authors proposed that the higher rate of H_2 generation may have been attributable to changes in speciation of dissolved Fe following the pH increase. Specifically, they proposed that at higher pH a greater proportion of dissolved Fe would have been present as $FeOH^+$, and more rapid oxidation of this species relative to other dissolved Fe compounds may have allowed increased production of dissolved Fe^{III} species, leading in turn to more rapid precipitation of magnetite and increased H_2 generation. Yet, higher pH did not lead to magnetite precipitation in the lherzolite experiment of Seyfried et al. (2007), and olivine serpentinization experiments conducted at strongly alkaline pH resulted in a smaller fraction of Fe being partitioned into magnetite rather than into serpentine and brucite when compared with reactions under mildly alkaline conditions (McCollom et al., 2020). Both of the latter results disagree with expectations if oxidation of $FeOH^+$ was driving increased magnetite formation. A possible alternative explanation for the steep increase in H_2 production rate observed by Syverson et al. (2017) is that it was attributable to higher overall rates of olivine reaction following the pH increase, similar to the increased reaction rates at higher pH observed in OlivOpx230 and the olivine serpentinization experiments of McCollom et al. (2020). That is, an increase in the overall rate of olivine reaction would be expected to generate a higher flux of H_2 even if the proportion of Fe^{III} produced from each increment of olivine remains the same (or even if it decreases somewhat; McCollom et al., 2020), so an increase in the proportion of $FeOH^+$ converted to magnetite is not required to explain the higher rate of H_2 generation.

4.7. Implications for natural systems

The flux of H_2 that is discharged from actively serpentinizing systems is strongly dependent on both the overall rate of serpentinization and the partitioning of Fe^{III} into the reaction products (Rxn. 1), among other factors. The results of this study together with those of McCollom et al. (2020) indicate that the transition of serpentinizing systems from mildly alkaline to strongly alkaline conditions is accompanied by a sharp increase in overall reaction rate, resulting in a concurrent increase in rate of H_2 production. Changes in the partitioning of Fe^{III} among the reaction products at higher pH appears to make a lesser contribution to the increased amount of H_2 production than the overall reaction rate, and the total amount of H_2 generated from each increment of rock undergoing serpentinization may even decrease somewhat with increasing pH

Table 6
Comparison of net amount of H_2 generated per gram reactants undergoing reaction in OlivOpx230 and the olivine-only experiment Oliv230pH from McCollom et al. (2020).

	OlivOpx230	Oliv230pH
Amount of H_2 generated per g reactants (μmol)	91	105
Percent reactants converted to products	53	70
Net amount of H_2 generated from each g reactant converted to products (μmol)	175	150

(McCollom et al., 2020). The overall outcome is that, other environmental factors being equal, serpentinization at higher pH should produce higher H_2 concentrations in discharged fluids, although the increased rate of reaction means that the higher concentrations would be sustained for a shorter period of time before the rock is fully serpentinized. Ultimately, the net total amount of H_2 generated from a given mass of rock during serpentinization may not vary appreciably as a function of pH, it will just get generated over a shorter span of time under increasingly alkaline conditions.

The experiments reported here as well as other laboratory studies (e.g., Seyfried et al., 2007; Grozeva et al., 2017; Syverson et al., 2017) indicate that the transition to strongly alkaline pH and onset of significant H_2 production may not occur immediately as fresh rocks begin to undergo serpentinization. Instead, the earliest stage of serpentinization may result in only mildly alkaline pH and low H_2 concentrations, as well as relatively slow serpentinization rates. If the model results in Fig. 5 are representative, these conditions may persist until a significant fraction (~15% or more) of the rock is serpentinized. These observations suggest that circumneutral fluids which circulate through ultramafic rocks in the early stages of serpentinization may emerge with compositions that lack the characteristics typically associated with serpentinizing systems (e.g., strongly alkaline pH, elevated H_2 concentrations, and low SiO_2). Such fluids might not be readily recognized as the product of fluid-rock interaction with ultramafic rocks, and their association with serpentinization in the subsurface could be overlooked.

Although the available experimental data are limited, the results of this study also suggests that the net amount of H_2 generated from each increment of serpentinized rock may be less dependent on initial rock composition than on other factors such as temperature. For example, the amount of H_2 generated per gram of reacted minerals was similar for the olivine-Opx mixture in OlivOpx230 and for reaction of olivine by itself under comparable conditions (Table 6), even though the H_2 was predominantly generated from incorporation of Fe^{III} into magnetite in OlivOpx230 and into serpentine in the olivine-only experiment (Supplemental Table S3). Thermodynamic models also predict that serpentinization should produce roughly the same amount of H_2 from a given mass of rock for protolith compositions ranging from dunites to harzburgites and lherzolites when reacted at the same temperature (Klein et al., 2013).

Lastly, the experimental results have potential implications for the interpretation of dissolved SiO_2 concentrations from lower temperature (<250 °C) serpentinizing systems, such as the Lost City deep-sea hydrothermal system on the Mid-Atlantic Ridge. Fluids discharged from hydrothermal vents at Lost City are strongly alkaline (pH up to 11) and contain highly elevated H_2 concentrations, reflecting interaction with serpentinizing rocks in the subsurface (e.g., Kelley et al., 2005). Although the fluids are discharged at the seafloor with temperatures around 90 °C, it is thought that their compositions are regulated by fluid-rock interactions at temperatures closer to 200 °C in the subsurface (Proskurowksi et al., 2006; Foustoukos et al., 2008), so that the source regions have temperatures similar to the experiments in this study.

The hydrothermal fluids at Lost City have ΣSiO_2 concentrations in the 24–73 μM range (Seyfried et al., 2015). These concentrations are well above those expected for serpentine-brucite equilibrium, giving rise to discussions about what reactions might regulate the SiO_2 levels. For instance, Seyfried et al. (2015) hypothesized that ΣSiO_2 concentrations may be controlled by equilibrium with the mineral assemblage serpentine + diopside + tremolite owing to the presence of plagioclase in subsurface reaction zones. Alternatively, Tutolo et al. (2018) proposed that slow kinetics for reaction of dissolved SiO_2 with brucite to form serpentine may be responsible for the relatively high ΣSiO_2 concentrations.

Results of this study suggest that another possible explanation for the ΣSiO_2 concentrations in Lost City fluids is that they are regulated by reactions taking place at the surface of dissolving olivine (Rxn. 6), similar to the reactions proposed for the laboratory experiments. The ΣSiO_2 concentrations throughout Stage III of OlivOpx230 (46–115 mmol kg^{-1}) and during the olivine-only experiments conducted at the same temperature (17–71 mmol kg^{-1}; McCollom et al., 2016) overlap those observed at Lost City, and these levels were maintained for extended periods of time during the experiments. The persistence of ΣSiO_2 concentrations in the experiments at levels similar to those observed at Lost City suggests that similar mechanisms may be involved in regulating the abundance of dissolved SiO_2, and demonstrate that neither plagioclase nor brucite need be present in the reaction zone to account for the ΣSiO_2 concentrations at Lost City. The possibility that reactions occurring on the surface of dissolving olivine might regulate ΣSiO_2 concentrations at Lost City and in other low temperature serpentinizing systems merits further investigation.

5. CONCLUSIONS

The transition from mildly alkaline to strongly alkaline conditions during experimental serpentinization of an olivine-Opx mixture was found to produce steep increases

in overall reaction rate and generation of H_2, providing additional support for the proposition that the rate of serpentinization increases with increasingly alkaline pH (McCollom et al., 2020). The higher rate of H_2 generation at elevated pH is primarily driven by the higher overall rate of reaction (i.e., more increments of the reactant minerals serpentinized during a given interval of time) with only relatively minor changes in the amount of Fe^{III} produced from each increment of minerals reacted. Orthopyroxene was found to react more rapidly than olivine at the experimental conditions, both when the minerals were reacted alone and when they were included together in the same experiment. In addition, olivine in the presence of Opx reacted at a rate that was comparable to rates observed for olivine alone at similar pH, indicating that transfer of elements between reactant minerals did not significantly affect the rate of olivine reaction. The partitioning of Fe among the reaction products from experiment OlivOpx230 was found to be in reasonably good agreement with predictions from reaction path models, suggesting that thermodynamic equilibrium exerted a strong influence in determining how Fe was distributed among the secondary products as the reaction proceeded. The concentrations of ΣSiO_2 throughout the latter half of OlivOpx230 were maintained at levels consistent with metastable equilibrium between olivine and a brucite-like surface layer, suggesting that SiO_2 levels may have been regulated by reactions taking place on the surface of dissolving olivine.

Declaration of Competing Interest

The authors declare that they have no known competing financial interests or personal relationships that could have appeared to influence the work reported in this paper.

ACKNOWLEDGMENTS

This research was supported by the U. S. National Science Foundation Marine Geology and Geophysics program through grant NSF-OCE 0927744 and by the NASA Astrobiology Institute through Cooperative Agreement NNA15BB02A. Additional support to TMM from the Hanse Wissenschaftskolleg (Delmenhorst, Germany) at an early stage of this project is gratefully acknowledged. FK acknowledges support through Grant NSF-OCE 1427274. The IRM is supported by the Instruments and Facilities Program of the NSF Division of Earth Science. This is IRM contribution 1711. We very much appreciate the comments of Fabrice Brunet, Gleb Pokrovski and an anonymous reviewer that helped us refine our interpretations and improve communication of the results.

APPENDIX A. SUPPLEMENTARY MATERIAL

Supplementary data to this article can be found online at https://doi.org/10.1016/j.gca.2020.05.016.

REFERENCES

Bach W., Paulick H., Garrido C. J. and Ildefonse B. (2006) Unraveling the sequence of serpentinization reactions: petrography, mineral chemistry, and petrophysics of serpentinites from MAR 15°N (ODP Leg 209, Site 1274). *Geophys. Res. Lett.*. https://doi.org/10.1029/2006GL025681.

Berndt M. E., Allen D. E. and Seyfried, Jr., W. E. (1996) Reduction of CO_2 during serpentinization of olivine at 300°C and 500 bar. *Geology* **24**, 351–354.

Bethke C. M. (2008) *Geochemical and Biogeochemical Reaction Modeling*. Cambridge University Press, p. 543.

Bonnemains D., Carlut J., Escartín J., Mével C., Andreani M. and Debret B. (2016) Magnetic signatures of serpentinization at ophiolite complexes. *Geochem. Geophys. Geosyst.* **17**. https://doi.org/10.1002/2016GC006321.

Braithwaite R. S. W., Dunn P. J., Pritchard R. G. and Paar W. H., Iowaite, a re-investigation. Mineral. Mag.58, 1994, 79-85.

Closmann C., Knittle E. and Bridges F. (1996) An XAFS study of the crystal chemistry of Fe in orthopyroxene. *Am. Mineral.* **81**, 1321–1331.

Evans B. W. and Trommsdorf V. (1972) Die einfluss des eisens auf die hydratisierung von duniten. *Schweiz. Min. Pet. Mitt.* **52**, 251–256.

Evans B. W. (2008) Control of the products of serpentinization by the $Fe^{+2}Mg_{-1}$ exchange potential of olivine and orthopyroxene. *J. Petrol.* **49**, 1873–1887.

Foustoukos D. I., Savov I. P. and Janecky D. R. (2008) Chemical and isotopic constraints on water/rock interactions at the Lost City hydrothermal field, 30°N Mid-Atlantic Ridge. *Geochim. Cosmochim. Acta* **72**, 5457–5474.

Frost B. R. and Beard J. S. (2007) On silica activity and serpentinization. *J. Petrol.* **48**, 1351–1368.

Grozeva N. G., Klein F., Seewald J. S. and Sylva S. P. (2017) Experimental study of carbonate formation in oceanic peridotites. *Geochim. Cosmochim. Acta* **199**, 264–286.

Huang R., Song M., Ding X., Zhan W. and Sun W. (2017a) Influence of pyroxene and spinel on the kinetics of peridotite serpentinization. *J. Geophys. Res.* **122**, 7111–7126.

Huang R., Lin C.-T., Sun W., Ding X., Zhan W. and Zhu J. (2017b) The production of iron oxide during peridotite serpentinization: Influence of pyroxene. *Geosci. Front.* **8**, 1311–1321.

Janecky D. R. and Seyfried, Jr., W. E. (1986) Hydrothermal serpentinization of peridotite within the oceanic crust: Experimental investigations of mineralogy and major element chemistry. *Geochim. Cosmochim. Acta* **50**, 1357–1378.

Kelley D. S., Karston J. A., Früh-Green G. L., Yoerger D. R., Shank T. M., Butterfield D. A., Hayes J. M., Schrenk M. O., Olson E. J., Proskurowski G., Jakuba M., Bradley A., Larson B., Ludwig K., Glickson D., Buckman K., Bradley A. S., Brazelton W. J., Roe K., Elend M. J., Delacour A., Bernasconi S. M., Lilley M. D., Baross J. A., Summons R. E. and Sylva S. P. (2005) A serpentinite-hosted ecosystem: The Lost City hydrothermal field. *Science* **307**, 1428–1434.

Klein F., Bach W., Jöns N., McCollom T. M., Moskovitz B. and Berquo T. (2009) Iron partitioning and hydrogen generation during serpentinization of abyssal peridotites from 15°N on the Mid-Atlantic Ridge. *Geochim. Cosmochim. Acta* **73**, 6868–6893.

Klein F., Bach W. and McCollom T. M. (2013) Compositional controls on hydrogen generation during serpentinization of ultramafic rocks. *Lithos* **99**, 377–386.

Klein F., Bach W., Humphris S. E., Kahl W. A., Jöns N., Moskowitz B. and Berquó T. (2014) Magnetite in seafloor serpentinite - some like it hot. *Geology* **42**, 135–138.

Klein F., Grozeva N. G., Seewald J. S., McCollom T. M., Humphris S. E., Moskovitz B., Berquo T. S. and Kahl W.-A. (2015) Experimental constraints on fluid-rock interactions during incipient serpentization of harzburgite. *Am. Mineral.* **100**, 991–1002.

Klein F. and Le Roux V. (2020) Quantifying the volume increase and chemical exchange during serpentinization. *Geology* **48**. https://doi.org/10.1130/G47289.1.

Lafay R., Montes-Hernandez G., Janots E., Chiriac R., Findling N. and Toche F. (2012) Mineral replacement rate of olivine by chrysotile and brucite under high alkaline conditions. *J. Crystal Growth* **347**, 62–72.

Malvoisin B., Brunet F., Carlut J., Rouméjon S. and Cannat M. (2012a) Serpentinization of oceanic peridotites: 1: A high-sensitivity method to monitor magnetite production in hydrothermal experiments. *J. Geophys. Res.* **117**, B01104. https://doi.org/10.1029/2011JB008612.

Malvoisin B., Brunet F., Carlut J., Rouméjon S. and Cannat M. (2012b) Serpentinization of oceanic peridotites: 2. Kinetics and processes of San Carlos olivine hydrothermal alteration. *J. Geophys. Res.* **117**. https://doi.org/10.1029/2011JB008842.

Marcaillou C., Muñoz M., Vidal O., Parra T. and Harfouche M. (2011) Mineralogical evidence for H_2 degassing during serpentinization at 300 °C/300 bar. *Earth Planet. Sci. Lett.* **303**, 281–290.

Martin B. and Fyfe W. S. (1970) Some experimental and theoretical observations on the kinetic of hydration reactions with particular reference to serpentinization. *Chem. Geol.* **6**, 185–202.

Mayhew L. E. and Ellison E. T. (2020) A synthesis and meta-analysis of the Fe chemistry of serpentinites and serpentine minerals. *Phil. Trans. Roy. Soc. A.* **378**, 20180420.

McCollom T. M. and Bach W. (2009) Thermodynamic constraints on hydrogen generation during serpentinization of ultramafic rocks. *Geochim. Cosmochim. Acta* **73**, 856–875.

McCollom T. M. and Seewald J. S. (2001) A reassessment of the potential for reduction of dissolved CO_2 to hydrocarbons during serpentinization of olivine. *Geochim. Cosmochim. Acta* **65**, 3769–3778.

McCollom T. M. and Seewald J. S. (2007) Abiotic synthesis of organic compounds in deep-sea hydrothermal environments. *Chem. Rev.* **107**, 382–401.

McCollom T. M. and Seewald J. S. (2013) Serpentinites, hydrogen, and life. *Elements* **9**, 129–134.

McCollom T. M. (2016) Abiotic methane formation during experimental serpentinization of olivine. *Proc. Nat. Acad. Sci. USA* **113**, 13965–13970.

McCollom T. M., Klein F., Robbins M., Moskowitz B., Berquó T. S., Jöns N., Bach W. and Templeton A. (2016) Temperature trends for reaction rates, hydrogen generation, and partitioning of iron during experimental serpentinization of olivine. *Geochim. Cosmochim. Acta* **181**, 175–200.

McCollom T. M., Klein F., Solheid P. and Moskowitz B. (2020) The effect of pH on rates of reaction and hydrogen generation during serpentinization. *Phil. Trans. Roy. Soc. A.* **378**, 20180428.

Moody J. B. (1976a) An experimental study on the serpentinization of iron-bearing olivines. *Can. Mineral.* **14**, 462–478.

Moody J. B. (1976b) Serpentinization: a review. *Lithos* **9**, 125–138.

Oelkers E. H. and Schott J. (2001) An experimental study of enstatite dissolution rates as a function of pH, temperatures, and aqueous Mg and Si concentration, and the mechanism of pyroxene/pyroxenoid dissolution. *Geochim. Cosmochim. Acta* **65**, 1219–1231.

Oelkers E. H., Declerq J., Saldi G. D., Gislason S. R. and Schott J. (2018) Olivine dissolution rates: A critical review. *Chem. Geol.* **500**, 1–19.

Ogasawara Y., Okamoto A., Hirano N. and Tsuchiya N. (2013) Coupled reactions and silica diffusion during serpentinization. *Geochim. Cosmochim. Acta* **119**, 212–230.

Okamoto A., Ogasawara Y., Ogawa Y. and Tsuchiya N. (2011) Progress of hydration reactions in olivine-H_2O and orthopyroxenite-H_2O systems at 250 °C and vapor-saturated pressure. *Chem. Geol.* **289**, 245–255.

Oufi O., Cannat M. and Horen H. (2002) Magnetic properties of variably serpentinized abyssal peridotite. *J. Geophys. Res.* **107**, B5. https://doi.org/10.1029/2001JB000549.

Pokrovsky O. S. and Schott J. (2000) Kinetics and mechanism of forsterite dissolution at 25°C and pH from 1 to 12. *Geochim. Cosmochim. Acta* **64**, 3313–3325.

Proskurowksi G., Lilley M. D., Kelley D. S. and Olson E. J. (2006) Low temperature volatile production at the Lost City Hydrothermal Field, evidence from a hydrogen stable isotope geothermometer. *Chem. Geol.* **229**, 331–343.

Schrenk M. O., Brazelton W. J. and Lang S. Q. (2013) Serpentinization, carbon, and deep life. In *Carbon in Earth. Rev. Mineral. Geochem*, vol. 75 (eds. R. M. Hazen, A. P. Jones and J. Baross), pp. 575–606.

Seyfried, Jr., W. E. and Dibble, Jr., W. E. (1980) Seawater-peridotite interaction at 300°C and 500 bars: implications for the origin of oceanic serpentinites. *Geochim. Cosmochim. Acta* **44**, 309–321.

Seyfried, Jr., W. E., Janecky D. R. and Berndt M. E. (1987) Rocking autoclaves for hydrothermal experiments, II. The flexible reaction-cell system. In *Hydrothermal Experimental Techniques* (eds. G. C. Ulmer and H. L. Barnes). John Wiley and Sons, pp. 216–239.

Seyfried, Jr., W. E., Foustoukos D. I. and Fu Q. (2007) Redox evolution and mass transfer during serpentinization: An experimental and theoretical study at 200 °C, 500 bar with implications for ultramafic-hosted hydrothermal systems at Mid-Ocean Ridges. *Geochim. Cosmochim. Acta* **71**, 3872–3886.

Seyfried, Jr., W. E., Pester N. J., Tutulo B. M. and Ding K. (2015) The Lost City hydrothermal system: Constraints imposed by vent fluid chemistry and reaction path models on subseafloor heat and mass transfer processes. *Geochim. Cosmochim. Acta* **163**, 59–79.

Shibuya T., Yoshizaki M., Sato M., Shimizu K., Nakamura K., Omori S., Suzuki K., Takai K., Tsunakawa H. and Maruyama S. (2015) Hydrogen-rich hydrothermal environments in the Hadean ocean inferred from serpentinization of komatiites at 300 °C and 500 bar. *Prog. Earth Planet. Sci.* **2**, 46.

Syverson D. D., Tutolo B. M., Borrok D. M. and Seyfried, Jr., W. E. (2017) Serpentinization of olivine at 300 °C and 500 bars: An experimental study examining the role of silica on the reaction path and oxidation state of iron. *Chem. Geol.* **475**, 122–134.

Toft P. B., Arkani-Hamed J. and Haggerty S. E. (1990) The effects of serpentinization on density and magnetic susceptibility: a petrophysical model. *Phys. Earth Planet. Int.* **65**, 137–157.

Tutolo B. M., Luhmann A. J., Tosca N. J. and Seyfried, Jr., W. E. (2018) Serpentinization as a reactive transport process: The brucite silicification reaction. *Earth Planet. Sci. Lett.* **484**, 385–395.

Ueda H., Sawaki Y. and Maruyama S. (2017) Reactions between olivine and CO_2-rich seawater at 300 °C: Implications for H_2 generation and CO_2 sequestration on the early Earth. *Geosci. Front.* **8**, 387–396.

Viti C. (2010) Serpentine minerals discrimination by thermal analysis. *Am. Mineral.* **95**, 631–638.

Wegner W. W. and Ernst W. G. (1983) Experimentally determined hydration and dehydration reaction rates in the system MgO-SiO_2-H_2O. *Am. J. Science* **283-A**, 151–180.

Wolery T. J. and Jarek R. L. (2003) *Software user's manual: EQ3/6, Version 8.0*. Lawrence Livermore National Laboratory, Livermore, Calif.

Associate editor: Gleb S. Pokrovski